Connecting sequence features within the disordered C-terminal linker of *B. subtilis* FtsZ to function and bacterial cell division

Min Kyung Shinn[a], Megan C. Cohan[a], Jessie L. Bullock[b], Kiersten M. Ruff [a,1], Petra A. Levin [b,1], Rohit V. Pappu[a,1]

[a] Department of Biomedical Engineering, Center for Science and Engineering of Living Cells (CSELS), Washington University in St. Louis, St. Louis, MO 63130

[b] Department of Biology, Washington University in St. Louis, St. Louis, MO 63130

[1]To whom correspondence may be addressed. Email: kiersten.ruff@wustl.edu, plevin@wustl.edu, pappu@wustl.edu

Keywords: Intrinsically disordered proteins; Autoregulation; Autoinhibition; Polymerization; Charge Patterning.

Classifications: Biochemistry; Biophysics and Computational Biology

Abstract (250 words)

Intrinsically disordered regions (IDRs) can function as autoregulators of folded enzymes to which they are tethered. One example of such a system is the protein FtsZ that controls cell division in bacteria. FtsZs include a folded core and a C-terminal tail (CTT). The latter encompasses a poorly conserved, disordered C-terminal linker (CTL) and a well-conserved 17-residue C-terminal peptide (CT17). Sites for GTPase activity of FtsZs are formed at the interface between GTP binding sites and T7 loops on cores of adjacent subunits within dimers. Here, we explore the basis of autoregulatory functions of the CTL plus CT17 in *Bacillus subtilis* FtsZ (*Bs*-FtsZ). Molecular simulations show that the CT17 of *Bs*-FtsZ makes statistically significant CTL-mediated contacts with the T7 loop. To test how CTL-mediated CT17-core contacts modulate subunit interactions and GTP hydrolysis, we designed *Bs*-FtsZ variants where we altered the patterning of oppositely charged residues within the CTL and assessed the effects on FtsZ assembly and function. Increasing the linear segregation of oppositely charged residues within the CTL disrupts core-CTT interactions. Mutations that enhance cohesive interactions among CTTs lead to alternative, tail-driven assemblies that diminish enzymatic activity. Altering the linear segregation of oppositely charged residues within the CTL can lead to protein degradation, aberrant assembly, and disruption of cell division *in vivo*. The functionally relevant non-random sequence patterns identified in this work are conserved across CTLs from orthologs. Our findings highlight how sequence patterns that contribute to functions can be uncovered in IDRs, including those with minimal sequence conservation.

Significance Statement (120 words)

Conserved sequence-structure-function relationships are the defining hallmarks of well-folded proteins. These relationships can be gleaned by combining multiple sequence alignments with covariation analyses. However, the approaches that work for well-folded proteins are not transferable to intrinsically disordered regions (IDRs) because their sequences vary dramatically across orthologs. Here, we use the C-terminal autoregulatory tail (CTT) of the bacterial cell division protein FtsZ to prototype a multi-pronged approach for studying IDRs. We show how

non-random sequence patterns within IDRs can be uncovered, analyzed for conservation, and redesigned to unmask their impact on molecular functions and cellular phenotypes. Through our work, we also introduce multi-pronged approaches that combine biophysical computations and biochemical experiments to understand how the CTT, as an IDR, functions.

Introduction

Intrinsically disordered regions contribute to a multitude of protein functions (1-4). A common occurrence is of autoregulatory IDRs tethered either as tails to folded domains or as linkers between folded domains (5-12). Of particular interest are IDRs tethered to folded domains that are enzymes (7, 13, 14). Several studies demonstrate that IDRs tethered to folded domains can function as autoregulators (12), specifically as autoinhibitors of enzymatic activities (13, 15, 16). One such example is the C-terminal tail (CTT) of the essential GTPase that controls and regulates bacterial cell division (17). The CTT encompasses a disordered C-terminal linker (CTL) and an alpha-helix-forming C-terminal peptide.

Cell division in bacteria is initiated by assembly of the cytokinetic ring at the nascent division site (18-26). Polymers formed by the essential GTPase **F**ilamenting **t**emperature-**s**ensitive mutant **Z** (FtsZ) are the foundation of this ring, which is also known as the Z-ring (27-32). A prokaryotic homolog of tubulin, FtsZ forms single-stranded protofilaments upon binding GTP *in vitro* (33). Linear polymers of FtsZ, which also undergo bundling via lateral associations, serve as a platform for the cell division machinery composed of at least thirty different proteins (19, 32, 34-39). FtsZ polymers also undergo treadmilling *in vivo*, driven by the turnover of subunits that occurs on the order of seconds (40).

Previous *in vitro* experiments showed that FtsZ polymerization belongs to a class of phase transitions known as reversible polymerization (41). As noted by Greer (41), a defining hallmark of reversible phase transitions, with subunit concentration as the conserved order parameter, is the presence of at least one threshold concentration for the occurrence of a specific phase transition. Cohan et al., recently identified two distinct threshold concentrations for *B. subtilis* FtsZ (*Bs*-FtsZ) phase transitions occurring in the presence of GTP (17). In agreement with previous work on *E. coli* FtsZ, *Bs*-FtsZ forms single-stranded protofilaments when the first threshold concentration, denoted as c_A, is crossed (42-47). The second threshold concentration, denoted as c_B where $c_B > c_A$, characterizes the threshold for bundling of protofilaments.

Bs-FtsZ encompasses two domains: a folded N-terminal core and a C-terminal tail (CTT) (**Figure 1A**). The core domain forms a complete GTPase upon dimerization whereby the T7 loop of one protomer is inserted into the nucleotide binding site of the complementary protomer. The interface between the T7 loop and the nucleotide binding site is the active site for GTP hydrolysis (48). The CTT is further composed of an intrinsically disordered C-terminal linker (CTL) and a 17-residue C-terminal peptide (CT17). The CT17 was previously termed CTP (17). It includes a conserved "constant region" and "variable region (CTV)" (30, 49, 50). CT17 can form alpha-helical conformations (51-53) and is thus an alpha-molecular recognition element (54) that enables a precise network of homotypic and heterotypic protein-protein interactions. Whereas CT17 includes a conserved region (55), the CTL is hypervariable across orthologs, varying in length, amino acid composition, and sequence (33, 49, 56, 57). Defects in the CTL and the CTV of *Bs*-FtsZ disrupt lateral interactions between protofilaments (49, 57).

Consistent with previous work (58-60), Cohan et al., showed, through systematic deletions of each module, that the core domain of *Bs*-FtsZ is the main driver of GTP binding induced

polymerization (17). Deletion of the CT17 (ΔCT17, previously referred to as ΔCTP) increases c_A while also shifting c_B upward by at least three-fold. Internal deletion of the CTL (ΔCTL) decreases c_A and this construct forms mini rings stabilized by cohesive interactions of the CT17. Overall, the CTL weakens the driving forces for linear polymerization and bundling, whereas the CT17 appears to be the primary driver of lateral associations. Deletion of the CTT (ΔCTT) lowers c_A by over an order of magnitude and forms long, single-stranded polymers. Cohan et al., also showed that ΔCTT is the most efficient GTPase, whereas the wild-type *Bs*-FtsZ is the least efficient enzyme of the four constructs studied (17).

The picture that emerges is of the CTT as an autoregulator of *Bs*-FtsZ assembly and an autoinhibitor of enzymatic activity (17). Here, we uncover a molecular-level, mechanistic understanding of how the distinctive functions of CTTs are achieved. We utilized atomistic simulations to uncover inter-module interactions among the CTL, CT17, and the core. Additionally, we deployed the recently developed NARDINI algorithm (61) to identify non-random sequence patterns within the CTL of *Bs*-FtsZ that contribute to inter-module interactions. In a large-scale NARDINI analysis of over 10^3 FtsZ orthologs, we identified conserved sequence patterns in CTLs that prevail despite the absence of sequence conservation. One conserved pattern is the linear segregation of negatively charged residues within the CTL. In contrast, the positively charged residues tend to be more randomly distributed along the linear sequences of CTLs. We designed a series of CTL variants of *Bs*-FtsZ by changing the degree of segregation / mixing of oppositely charged residues (61, 62). We experimentally evaluated the impact of altering the patterning of oppositely charged residues within the CTL of *Bs*-FtsZ on FtsZ assembly, enzymatic activity, cell growth, and cell division. We find that extreme segregation or mixing of oppositely charged residues within the CTL adversely affects FtsZ functionalities. These effects can be attributed to changes in interactions between the core domain and the CTT. We also find that changes to sequence patterns with in the CTL can alter FtsZ assembly dynamics and lead to mis-localization *in vivo*. Evolutionary analysis shows that FtsZs maintain optimal sequence patterns within disordered CTLs despite significant variations in sequence compositions and lengths. Taken together, our results highlight the importance of maintaining optimal sequence patterns within the disordered CTL.

Results

The CTL and CT17 interact with the core domain at mutually exclusive sites: In contrast to the folded core, the CTT is not resolved in crystal structures. It is predicted to be disordered with IUPRED scores being above 0.5 for the entirety of the CTT (**Figure 1B**) (30, 63). We performed atomistic simulations to map conformational preferences of the isolated CTT peptide from *Bs*-FtsZ. These simulations show that the CTT of *Bs*-FtsZ samples a heterogenous ensemble of conformations with alpha-helical and random-coil character (**Figure 1C**). A large fraction of the alpha-helical signal arises from the CT17 suggesting that it is an example of an alpha-helical molecular recognition element / feature (α-MoRE or α-MoRF) (64, 65). Consistent with the predictions from simulations, ultraviolet circular dichroism (UV-CD) measurements for the isolated CTT peptide indicate that it is conformationally heterogeneous (Figs. **1D,** *SI Appendix*, **Figure S1**).

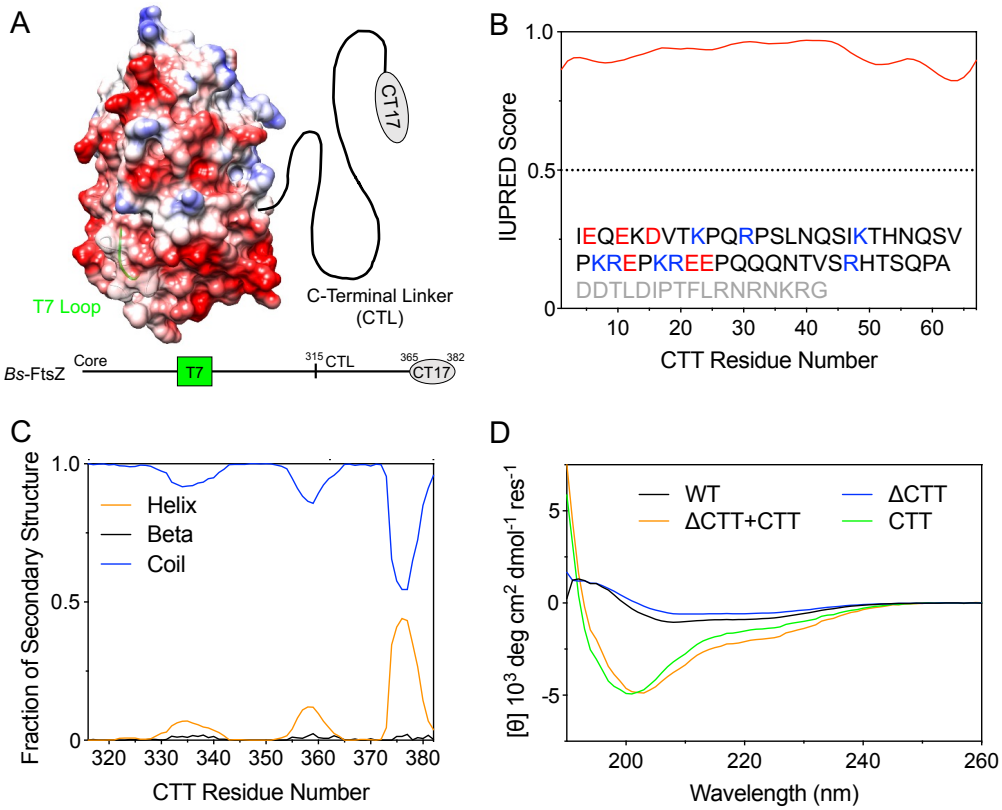

Figure 1: **Modular architecture of *B. subtilis* FtsZ includes a disordered CTT.** (A) The electrostatic potential (66) is mapped onto the core domain in red and blue for regions of negative and positive potential, respectively. The T7 loop is highlighted in green. The CTT includes C-terminal linker (CTL) that connects the 17-residue C-terminal peptide (CT17) to the core domain. (B) The CTT is predicted to be disordered using IUPRED (63). The CTT sequence is shown with negatively and positively charged residues of the CTL in red and blue, respectively. The CT17 sequence is shown in gray. (C) Average secondary structure contents of the CTT as predicted by atomistic simulations. (D) UV-CD spectra of the four *Bs*-FtsZ constructs.

The CD spectrum for the ΔCTT construct, which refers to the core domain without the CTT, is consistent with a mixture of structures with minima at 208 and 222 nm, indicating the presence of alpha-helical and beta-sheet structures. The spectrum of full-length FtsZ closely resembles that of the ΔCTT construct with a mixture of structures. The sum of the spectra for the core domain and the CTT does not reproduce the spectrum of a full-length protein. This suggests that the CTT likely undergoes conformational changes when it is tethered to the core domain by forming inter-module interactions with the core.

We also performed atomistic simulations of the full-length wild-type (WT) *Bs*-FtsZ protomer to investigate the presence and types of interactions among the core domain, the CTL, and the CT17. The core-CTL and core-CT17 interactions were defined by the presence of residues within the CTL or CT17 being within 10 Å of a core residue. The frequencies of contacts were calculated from simulations and are shown as a heatmap, with regions where contacts are made being annotated on the structure of the core domain. The CT17 fluctuates into and out of making contacts with the T7 loop (**Figure 2A**), whereas contacts between the CTL and the core exclude the T7 loop and mainly involve residues that are spatially proximal to the region on the core where

the CTT is N-terminally tethered (**Figure 2C**). Synergies between core-CTL and core-CT17 interactions were definitively unmasked in simulations of the different deletion constructs *viz*., the ΔCTL and ΔCT17 that were studied by Cohan et al., (17). The CT17 does not interact with the T7 loop when the CTL is deleted. Instead, alternate contacts form with the residues that are spatially proximal to the site where the CT17 is N-terminally tethered to the core domain in the ΔCTL construct (**Figure 2B**). Conversely, when the CT17 is deleted, the interactions between the CTL and the core that form in the full-length WT *Bs*-FtsZ protomer are preserved. Additionally, there are statistically significant contacts between the CTL and the T7 loop in the absence of the CT17.

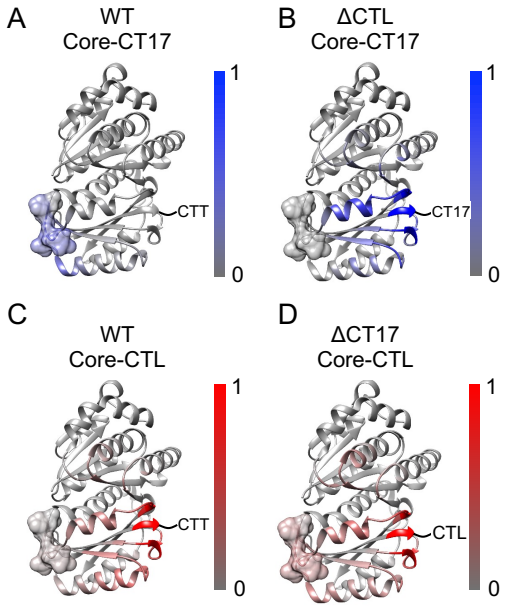

Figure 2: The CT17 and the CTL interact with mutually exclusive sites on the surface of the core domain. Color bars show the contact frequency between the core and (A, B) CT17 (blue) or (C, D) CTL (red) in WT, ΔCTL, and ΔCT17 constructs. The T7 loop is shown in space-filling model. The C-terminus of the core domain where the CTT emanates is noted.

Overall, the simulations show that the CTL and the CT17 can compete for interactions with the T7 loop of the core domain. However, in the full-length protomer, interactions between the CT17 and the T7 loop are favored over those with the CTL. Thus, the CTL becomes the facilitator of distal contacts between the CT17 and the T7 loop of the core domain. These results suggest the presence of "on" and "off" states whereby in the "on" state, the CT17 occupies the T7 loop, and in the "off" state, the CT17 is dissociated from the T7 loop.

Identifying non-random sequence patterns within the Bs-FtsZ CTL: Next, we asked if there are non-random sequence patterns within the CTL. Our goal was to identify sequence patterns that are likely facilitators of CTT interactions with the core, not just in *Bs*-FtsZ, but also in orthologs. For this, we utilized the recently described NARDINI algorithm to analyze the CTL of *Bs*-FtsZ and extract non-random binary patterns (67). NARDINI quantifies the extents of mixing vs. segregation of different pairs of amino acid types and ascribes a *z*-score to each of the binary patterns. A binary pattern is deemed to be non-random if the associated *z*-score meets the criteria of $-1.5 < z_{xy}$ or $z_{xy} > 1.5$, where xy refers to a specific pair of residue types. This analysis shows that the CTL of *Bs*-FtsZ is characterized by non-random segregation of polar residues x ≡ (Gln, Ser, Thr, Asn, His) with respect to negatively charged residues y ≡ (Asp, Glu), positively charged

residues y ≡ (Arg, Lys), and proline residues (**Figure 3A**). Additionally, negatively charged residues are also non-randomly segregated with respect to all other residue types. The segregation of polar and negatively charged residues appears to explain the observed statistically significant, albeit weak interactions with the core (**Figure 2**). Clusters of negatively charged residues are likely to repel the acid-rich surface of the core (**Figure 1A**) whereas clusters of polar residues are likely to form weak interactions with the core. These features of the CTT, specifically the CTL, appear to be facilitators of the observed interactions between the T7 loop and CT17. Interestingly, positively charged residues are randomly distributed along the sequence of the CTL ($z_{++} < 1.5$), indicating a selection against clusters of positively charged residues that can interact favorably with the negatively charged surface of the core (**Figure 1A**).

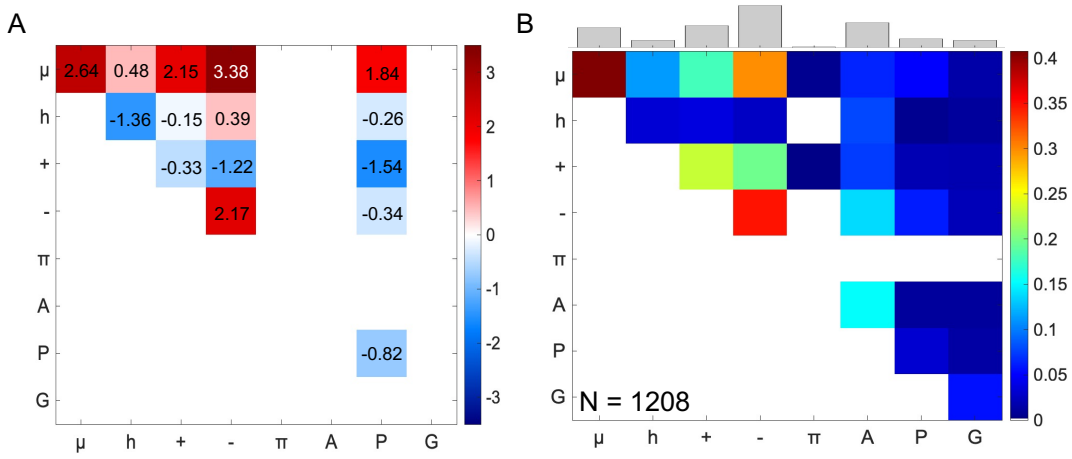

Figure 3: Uncovering non-random binary patterns in the *Bs*-FtsZ CTL and from CTLs across orthologs. (A) Z-score matrix for the CTL of *Bs*-FtsZ shows statistically significant non-random sequence patterns. Color bar indicates the z-scores. (B) Frequency of observing non-random segregation of different types of residue pairs ($z_{xy} > 1.5$) in CTLs from 1208 FtsZ orthologs. The histogram on top shows relative cumulative frequency of non-random features for segregation of each residue / residue type.

The CTL is hypervariable in length, amino acid composition, and sequence (33, 56). Despite this hypervariability, we find that several binary sequence patterns are conserved across CTLs derived from 1208 distinct FtsZ orthologs (*SI Appendix*, **Figure S2**). In accord with findings for *Bs*-FtsZ, we find that polar and negatively charged residues form linear clusters that are segregated from one another and all other residue types (**Figure 3B**). The NARDINI analysis highlights the conservation of linear clusters of negatively charged residues and clusters of polar residues. We propose that these features enable the preservation of statistically significant, albeit weak CTL-core interactions that enable inhibitory interactions through contacts between the CT17 peptide and the T7 loop. The corollary of our proposal is that disruption of these features, achieved by mixing or segregating oppositely charged residues will weaken native interactions or enhance non-native interactions, thus having deleterious consequences *in vitro* and *in vivo*. We tested this hypothesis using sequence design whereby we generated variants, each featuring CTLs with the same amino acid composition of the WT *Bs*-FtsZ while titrating the extent of mixing vs. segregation of oppositely charged residues within the CTL.

Design of C-terminal linker variants: It is well-known that IDRs where the oppositely charged residues are well-mixed in the linear sequence will prefer expanded, well-solvated conformations (62, 68, 69). Accordingly, CTLs with well-mixed oppositely charged residues in the linear sequence are expected to weaken native CTT-core interactions. Conversely, IDRs where

the oppositely charged residues are segregated with respect to one another have the potential to engage in strong non-native intra-CTL / intra-CTT interactions, non-native interactions with the FtsZ core, and non-native inter-CTL interactions between different FtsZ molecules.

The linear mixing / segregation of oppositely charged residues can be quantified using different parameters (62, 70, 71) including κ_{+-}, where $0 \leq \kappa_{+-} \leq 1$ (62). Oppositely charged residues that are uniformly mixed within a linear sequence will yield values of $\kappa_{+-} \approx 0$ whereas a separation of oppositely charged residues into discrete blocks will yield values of $\kappa_{+-} \approx 1$. To test the impact of the linear patterning of oppositely charged residues on FtsZ functionalities, we designed a set of CTL variants using the amino acid composition of the CTL from *Bs*-FtsZ. The designed sequences span a wide range of κ_{+-} values between 0.14 and 0.72 (*SI Appendix,* Table S1). The calculation of CTT κ_{+-} values includes both the CTL and CT17 modules. Each of the designed *Bs*-FtsZ variants are denoted as K*x*, where *x* is hundred times the κ_{+-} value of the CTT in question. The sequences of the core domain and the CT17 were not altered.

Increasing κ_{+-} of the CTT introduces intra-CTT interactions and enhances CTT-core interactions: We performed two types of simulations of the Kappa variants of *Bs*-FtsZ. In the first mode, we performed simulations of CTT variants as autonomous units. In the second mode, we interrogated the conformations accessible to full-length FtsZ molecules with the CTT tethered N-terminally to the core. Results from simulations in mode 1 show a decrease of ensemble-averaged radii of gyration (R_g) as κ_{+-} is increased (**Figure 4A**). This derives from the increased favorability of intra-CTT interactions between blocks of oppositely charged residues within the CTL as the segregation of oppositely charged residues is increased. We tested predictions from simulations by performing fluorescence correlation spectroscopy (FCS) measurements that quantify the ensemble-averaged hydrodynamic radii (R_h) of CTT peptides. We observe a clear one-to-one correspondence between the calculated R_g and measured R_h values. It follows, in accord with previous observations (62, 68, 72), that increasing the linear segregation of oppositely charged residues drives the compaction of IDRs through cohesive interactions within the IDRs.

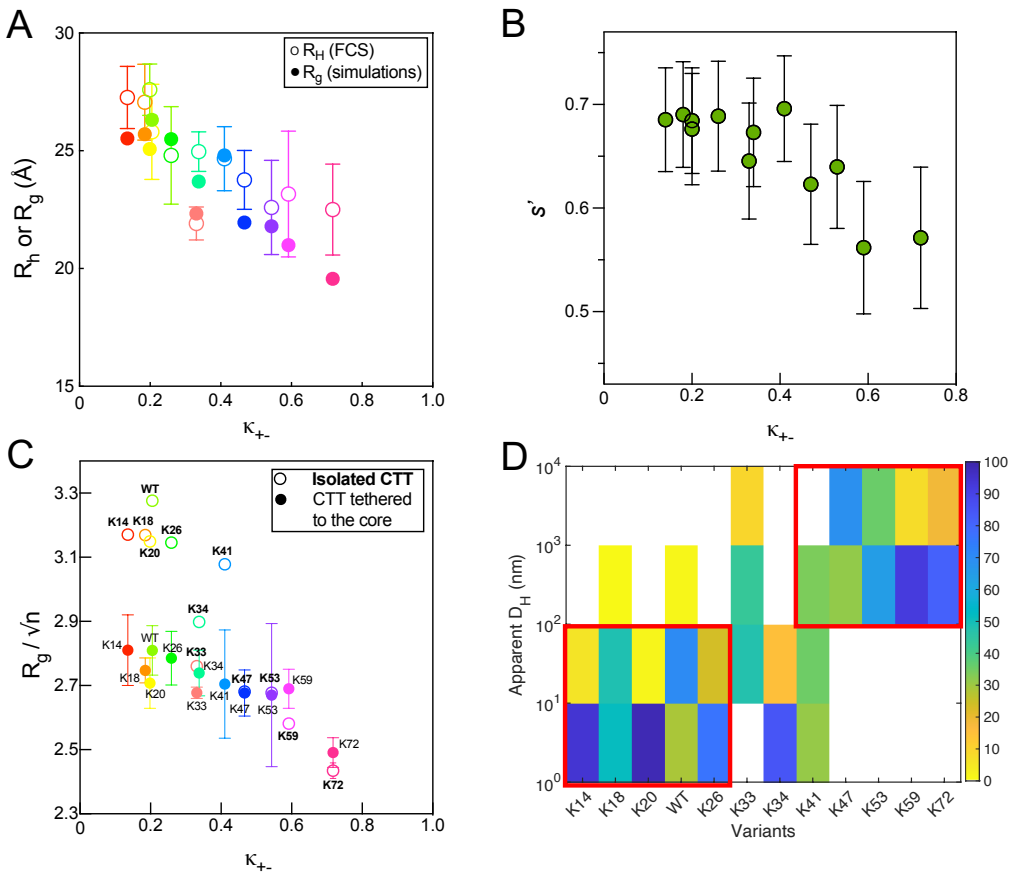

Figure 4: Increase in segregation of oppositely charged residues leads to compaction. (A) Computed R_g values from simulations and measured R_h values from FCS experiments as a function of κ_{+-} values of the Kappa variants. (B) Calculated Shannon entropy (s') values of the Kappa variants from computed R_g and δ^* values. (C) Normalized R_g of the Kappa variants from simulations in two modes, isolated (open symbols) and tethered to the GTPase core (solid symbols). CTT sequences with lower κ_{+-} values undergo compaction upon being tethered to the folded core. (D) DLS data, shown as a checkerboard plot that quantifies the percent likelihood of observing a scatterer of a specific size for each of the Kappa variants.

Two-dimensional histograms of normalized R_g and asphericity values of the CTT variants show evidence of conformational heterogeneity as manifest in the broad distribution of the sizes and shapes (56) (*SI Appendix*, **Figure S3**). We used these distributions to compute information theoretic measures of conformational heterogeneity such as relative Shannon entropies (s') (56) (**Figure 4B**). Despite a doubling of κ_{+-} from 0.20 and 0.41, the values of s' for the relevant CTT variants are bounded between 0.65 and 0.7. This implies that despite the decrease in R_g with increasing κ_{+-}, the overall conformational heterogeneity is not greatly impacted because enhancements in shape fluctuations offset any diminution in size fluctuations (56). However, we observe a clear reduction in s' values as κ_{+-} increases beyond 0.41.

Simulations of full-length proteins with the CTTs attached N-terminally to the core domain (**Figure 4C**) show that the CTT undergoes additional compaction for $\kappa_{+-} < 0.47$. This derives from contacts formed between the CTT and the core domain. However, this additional compaction is not observed in variants where the CTT κ_{+-} is greater than 0.41. This is because the interactions between oppositely charged blocky residues within the CTT are stronger than CTT-core

interactions as κ_{+-} increases beyond 0.41. This observation is supported by results from previous studies for other systems (8, 73).

Strong CTT-CTT interactions can drive FtsZ assemblies in vitro in the absence of GTP: Linear segregation of oppositely charged residues within the CTL introduces non-native interactions within the CTL. Additionally, this sequence feature has the potential to introduce non-native inter-domain interactions between the CTT and the core. We used dynamic light scattering (DLS) measurements of the different *Bs*-FtsZ variants to assess the contributions of non-native intermolecular interactions between FtsZ protomers. These measurements were made in the absence of GTP. Two groups of apparent hydrodynamic diameters (D_h) were observed (**Figure 4D**). Diameters smaller than 10^2 nm correspond to variants whose CTT κ_{+-} values are lower than 0.3. In contrast, D_h values larger than 10^2 nm were observed for *Bs*-FtsZ variants with CTT κ_{+-} values that are greater than 0.4. This increase in assembly size indicates a gain of non-native interactions arising from the altered features of the CTL.

The contributions of non-native CTT-CTT and CTT-core interactions to the overall FtsZ assembly in the absence of GTP can be inferred by quantifying correlations between D_h and the effective interaction strengths of CTT-CTT and CTT-core interactions. The weighted mean of the apparent D_h from DLS measurements was used as a quantitative proxy of the strengths of driving forces for *Bs*-FtsZ assembly in the absence of GTP. The effective strengths of CTT-CTT and the CTT-core interactions were extracted from statistical analysis of simulation results. First, the effective strengths $\varepsilon_{\text{inter-CTT}}$ of CTT-CTT interactions were determined by extracting R_g values for snapshots where the CTT is not in contact with the core. This helps us examine how strongly the CTT interacts with itself. The quantity of interest was defined as: $\varepsilon_{\text{inter-CTT}} = \left(\frac{R_{g,\max} - R_g}{R_{g,\max} - R_{g,\min}} \right)$ where R_g is the construct specific mean radius of gyration and $R_{g,\max}$ and $R_{g,\min}$ are the maximum and minimum values of the radii of gyration across κ_{+-} variants, respectively (**Figure 5A**). The derived values of $\varepsilon_{\text{inter-CTT}}$ are positively correlated with D_h (linear regression, $R^2 = 0.62$) indicating that inter-CTT interactions contribute to the FtsZ assembly in the absence of GTP. Second, the effective strengths of CTT-core interactions were calculated over snapshots where the CTT is in contact with the core using p_c, the mean per residue probability of finding any CTT residue in contact (5 Å) with any residue on the core in the simulated ensemble. Thus, p_c is large if many CTT residues interact with the core and the parameter of interest is defined as: $\varepsilon_{\text{core-CTT}} = \left(\frac{p_c - p_{c,\min}}{p_{c,\max} - p_{c,\min}} \right)$. Here, $p_{c,\max}$ and $p_{c,\min}$ are the maximum and minimum values of p_c across Kappa variants. The correlation between $\varepsilon_{\text{core-CTT}}$ and D_h is poor (linear regression, $R^2 = 0.21$). This implies that CTT-core interactions on their own make negligible contributions to the driving forces for FtsZ assembly in the absence of GTP (**Figure 5B**).

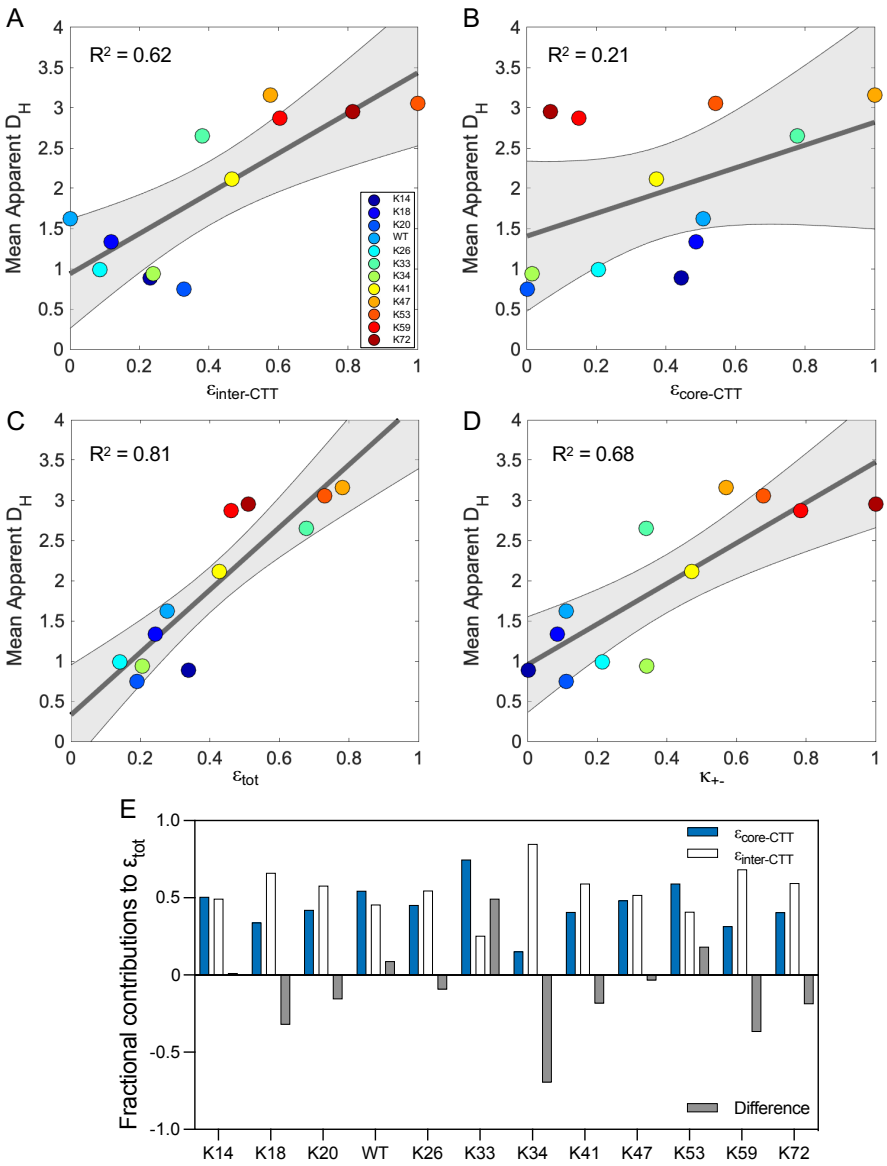

Figure 5: CTT-CTT and CTT-core interactions contribute to FtsZ assembly in the absence of GTP. Correlation between the mean apparent D_h measured using DLS and (A) $\varepsilon_{intra\text{-}CTT}$ (B) $\varepsilon_{core\text{-}CTT}$ (C) ε_{tot} and (D) κ_{+-}. Here, the grey area refers to the 95% confidence region of the linear regression. (E) Fractional contributions of $\varepsilon_{inter\text{-}CTT}$ (white bars) and $\varepsilon_{core\text{-}CTT}$ (blue bars) to ε_{tot}.

Next, we calculated the coupled contributions of the two parameters to GTP-independent assembly of FtsZ variants. For this, we used a Lever rule defined as: $\varepsilon_{tot} = f\varepsilon_{inter\text{-}CTT} + (1-f)\varepsilon_{core\text{-}CTT}$, where $0 \le f \le 1$. Here, f is the fraction of conformations in which the CTT is not in contact with the core. Joint consideration of the contributions of both types of interactions yields a strong positive correlation between ε_{tot} and D_h (linear regression, $R^2 = 0.81$) (**Figure 5C**) providing we extract a unique, Kappa-variant specific value of f (**Figure 5E**). The correlation between D_h and κ_{+-} is weaker than that between D_h and the total effective drive to assemble (linear regression $R^2 = 0.68$, **Figure 5D**). This is because κ_{+-} only describes the CTT-CTT interaction strength according to the positioning of oppositely charged residues, whereas the

Lever rule also accounts for the contributions of CTT-core interactions. Taken together, our results point to a combination of variant-specific CTT-CTT and CTT-core interactions as contributors to FtsZ assembly in the absence of GTP. CTT-core interactions within the Kappa variants are not identical even if the values of *f* are similar. For example, $f \sim 0.5$ for K14, WT, K26, and K47, and yet the interaction between the CT17 and the T7 loop is abolished in K47 (**Figure S4B**). Instead, we observe a gain of non-native CTL interactions with the T7 loop in this variant (**Figure S4A**). Overall, the pattern of non-native interactions will be influenced by the totality of non-random sequence patterns within the designed CTLs (**Figure 3**, *SI Appendix*, **Figure S2**).

Non-native interactions driven by redesigned CTLs promote large and diverse assemblies that are less active in GTP hydrolysis than WT: We investigated the effects of altered sequence patterns in the Kappa variants on GTP-dependent assembly and GTP hydrolysis. *In vitro*, *Bs*-FtsZ forms single-stranded protofilaments that associate laterally to form bundles (17, 49, 74-77). Right-angle light scattering is a sensitive method for studying FtsZ polymerization and bundling of FtsZ polymers in the presence of GTP (57). We measured scattering intensities of the Kappa variants and normalized these to measured values of WT for comparison. We observed two categories of variants using a 3-fold increase in scattering intensities when compared to WT as a threshold (**Figure 6A**). In general, the variants where the CTT κ_{+-} is ≤ 0.41 show lower scattering intensities and those with the CTT κ_{+-} values greater than 0.41 show higher scattering intensities. However, K18 is an exception. Despite having a CTT κ_{+-} value that is close to that of WT, the K18 variant exhibits high scattering intensities, indicating the formation of large assemblies.

Negative-stain transmission electron microscopy (TEM) imaging helps capture the diverse morphologies of higher-order assemblies formed by the Kappa variants (**Figure 6C**). Those that show lower scattering intensities correspond to protofilaments – see data for K14, K20, K33 (57), K41 – or rings composed of laterally associating bundled protofilaments (WT, K26). On the other hand, stronger non-native interactions driven by segregation of oppositely charged residues within the CTL lead to increased self-association of FtsZ variants via inter-CTT interactions among filaments. These interactions generate profoundly different assemblies when compared to morphologies observed for WT *Bs*-FtsZ (17, 30, 31, 78-80). Increase in the CTT κ_{+-} leads to the formation of long, linear filamentous tracts characterized by inter-filament interactions that appear to involve the CTTs – see data for K47, K53, K59, and K72 in **Figure 6C** and *SI Appendix*, **Figure S5**. These long FtsZ polymers are likely to compromise treadmilling thereby suppressing the exchange of FtsZ subunits in polymers upon GTP hydrolysis.

Next, we measured the rates of GTP hydrolysis of Kappa variants using a series of independent continuous assays for GTPase activity. Each measurement was performed with 5 μM FtsZ in buffer MES with 1 mM GTP. As with the right-angle scattering results, the Kappa variants can be grouped into two broad categories based on their GTPase activity relative to WT (**Figure 6B**). The concentration-specific GTPase activities are likely to be a convolution of many variables, including multiple assembly states of FtsZ and CTL-dependent variations to Michaelis-Menten parameters. However, at identical concentrations of FtsZ subunits, the sequence-encoded features within different CTLs directly influence the functions of the GTPase core domain with extreme segregation of oppositely charged residues reducing the GTPase activity.

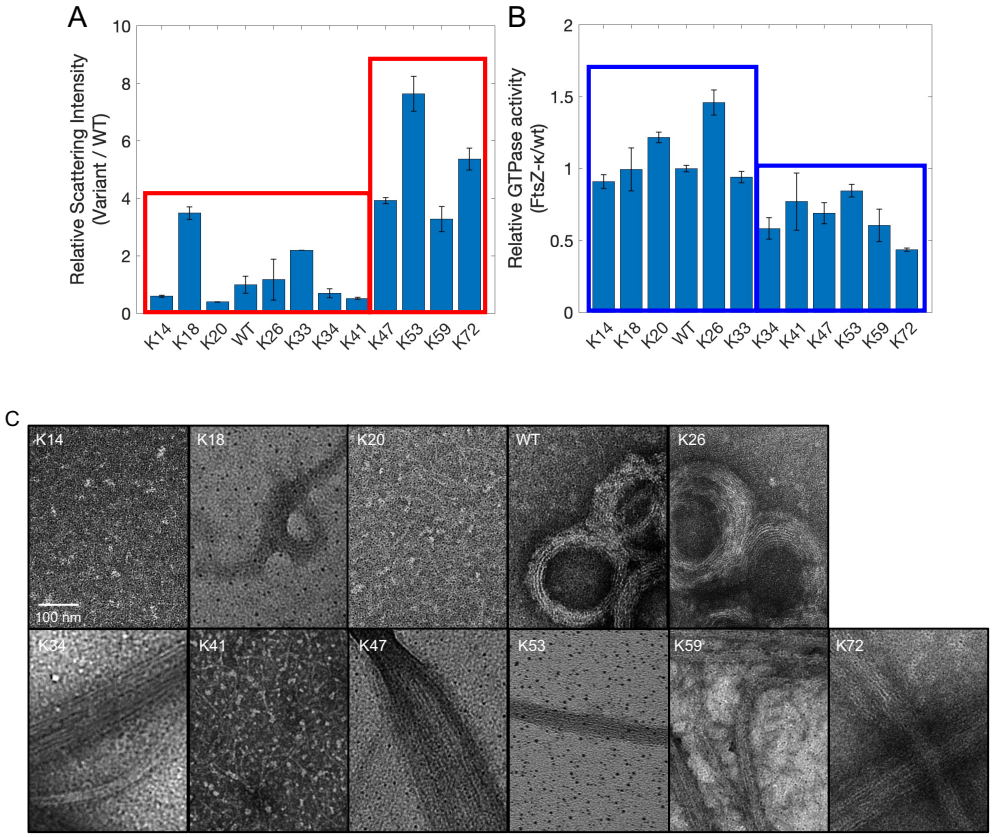

Figure 6: Changes to the patterning of oppositely charged residues within the CTL affects GTP-dependent FtsZ assembly and GTPase activity. (A) Scattering intensities of 5 μM of WT FtsZ and different variants were measured in the presence of 1 mM GTP. Values reported here were normalized to those of WT. The red outlines indicate two broad categories of the Kappa variants that show less than or more than 3-fold increase in scattering intensities compared to WT. (B) Rates of GTP hydrolysis of the Kappa variants are normalized to that of WT. Blue outlines indicate two broad categories of the Kappa variants that show faster, or slower rates compared to the WT. (C) Negative-stain TEM micrographs show the diverse morphologies formed by the Kappa variants.

Taken together, our results suggest that the linear sequence patterning, and the emergent native contacts lost or non-native contacts formed in *cis* (intra-CTL and CTT-core) and *trans* (CTT-CTT and CTT-core) can alter the functions of *Bs*-FtsZ variants. We find that extreme segregation or mixing of oppositely charged residues in the CTL cause significant deviations from WT-like behavior in FtsZ assembly and enzymatic activity *in vitro*. However, there is also robustness of both functions for CTT κ_{+-} values between 0.19 and 0.34.

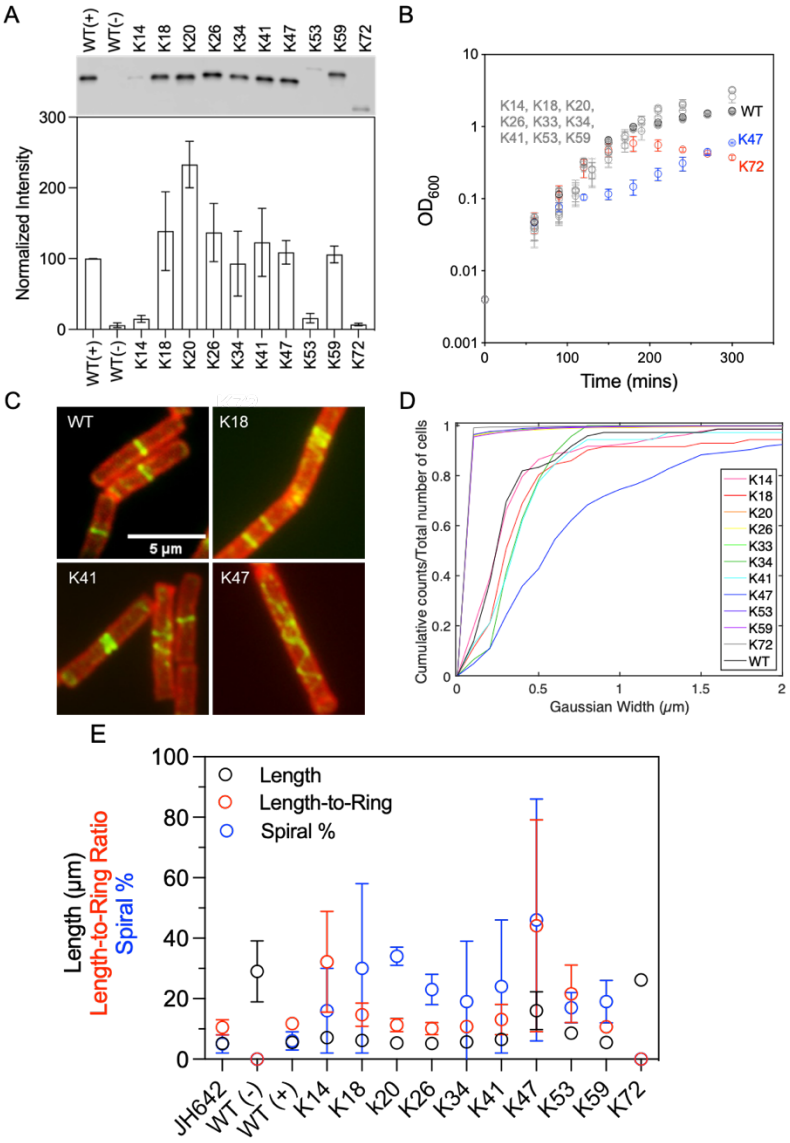

Figure 7: Changes to the extent of segregation vs. mixing of oppositely charged residues within the CTL affects protein stability, cell growth, and division. (A) Quantitative immunoblots of the Kappa variants. Intensities from the gel (top) are quantified in the histogram (below) and normalized to the WT. (B) Cell growth profiles of the Kappa variants. (C) In the IFM images, FtsZ is artificially colored in green, and the cell wall is in red. Scale bar = 2 µm. (D) The extent of condensation of FtsZ Kappa variants in cells is quantified using cumulative distribution functions. (E) We quantified cell lengths, length-to-ring ratios, and percentage of cells with spirals from the IFM images. Data for at least 200 cells were used for each of the Kappa variants. The L/R data for WT(-) and K72 were plotted at 0 since neither rings nor spirals were observed.

Extremes of mixing or segregation of oppositely charged residues also show pronounced in vivo phenotypes: In contrast to the assayed *in vitro* functionalities, *in vivo* functions of FtsZ are reliant on factors such as protein stability in the cell and interactions with other components of the division machinery. To evaluate *in vivo* functionalities of the Kappa variants, we used a strain that would allow us to examine variants as the sole copy of FtsZ regardless of their ability to support cell growth and division. This strain was made by cloning variant alleles into a *B. subtilis* strain

where the sole WT *ftsZ* gene is under the control of a xylose inducible promoter and the variant allele is under the control of an independent IPTG inducible promoter (42). We can then deplete WT FtsZ and induce the expression of the variants in a controlled manner.

We first evaluated the stability of FtsZ in cells using quantitative immunoblots since we observed notable changes in conformational ensembles with changes in CTT κ_{+-} values (**Figure 4C and** *SI Appendix***, Figure S3**), and it is reasonable to expect that changes to protein structure can lead to degradation *in vivo*. Samples were prepared from mid-exponential phase cultures (OD600 of ~0.5) that were back diluted into IPTG, then grown to and harvested at mid-exponential phase. Immunoblots were normalized to total protein levels. All but three variants accumulated near or above WT levels. The unstable variants are those with CTTs featuring extreme κ_{+-} values (**Figure 7A**) *viz*., K14, K53, and K72. These variants appear to be substantially degraded (< 20% WT FtsZ levels), indicating that they are more susceptible to proteolysis. Consistent with poor stability, strains expressing K72 were unable to support growth of *B. subtilis* (**Figure 7B**). In a clear contrast, the control strain (PAL3171) expressing only WT *ftsZ* under the IPTG inducible promotor exhibited a standard growth curve with exponential and stationary phases. As expected, the same control strain without *ftsZ* expression grew for approximately three hours before plateauing and slightly decreasing in optical density (81). Interestingly, all Kappa variants except for K47 and K72 exhibited robust WT-like growth profiles despite degradation of K14 and K53 in cells. Strains expressing K47 were able to support growth, but grew more slowly than the WT despite having FtsZ levels equivalent to WT. This suggests that K47 may interfere with both cross wall synthesis and synthesis of the longitudinal cell wall that leads to defects in growth.

To gain insight into FtsZ assembly *in vivo*, we used immunofluorescence microscopy (IFM) to quantify cell length and image FtsZ ring formation. Cultures were prepared as described for immunoblots, but harvested after roughly four doublings (OD600 of 1.5-0.3) for fixation and imaging (49). Here, longer cell lengths indicate impaired cell division. The three unstable variants, K14, K53, and K72, were 30%, 56% and 376% longer than WT, respectively (**Figure 7E,** *SI Appendix***, Figure S6**). Despite the high κ_{+-} value of its CTT, the average length of cells expressing K53 was like that of WT, while cells expressing the K18 allele were ~13% longer than WT cells. The variants with extreme segregation or mixing of the oppositely charged residues in their CTTs that exhibited longer cell lengths, also exhibited poor Z-ring formation. The Length-to-Ring ratio (L/R) metric was used to evaluate the ability of FtsZ to form Z-rings, and is defined as the ratio between the cumulative length of all measured cells and the cumulative numbers of rings in those cells (82). K14 and K47 showed higher L/R ratios, K72 was unable to form any rings, whereas K59, despite the higher κ_{+-} value of the CTT showed robust WT-like protein stability, cell growth profile, cell length, and L/R.

Images of cells expressing Kappa variants revealed the presence of unusual FtsZ localization patterns in many of the strains (**Figure 7C**). WT FtsZ forms well-defined medial rings with residual localization at cell poles. In contrast, most variants displayed loose, spiral-like structures in addition to distinct rings. Previous work identified spirals as being indicative of defects in lateral interactions between single stranded polymers which interferes with condensation into precisely localized Z-rings (83-86). Accordingly, we quantified the spiral phenotype by quantifying the percentage of cells with spirals. This quantity, which we termed Spiral %, was higher in all variants when compared to cells expressing only WT *Bs*-FtsZ. We also computed, the Gaussian width (**Figure 7D**), which is a measure of spiral width relative to cell length. Spiral formation was independent of FtsZ levels, cell length, and L/R ratios. Only K72 lacked spirals

possibly due to having insufficient levels of FtsZ for assembly (**Figure 7A**). This suggests that the Kappa variants are unable to condense efficiently. Instead, deviation from WT-like sequence patterns leads to a mixture of rings and spiral structures. The latter are likely to intermediate states that represent defects in condensation and / or localization.

Discussion

FtsZ plays an essential role in scaffolding the cell division machinery in rod-shaped bacteria, and this is accomplished in part by contributions of the C-terminal tail (CTT). The CTT contains an intrinsically disordered C-terminal linker (CTL) that connects the C-terminal peptide (CT17) to the GTPase core domain. Together, the CTL and CT17 act as autoregulators of GTPase activity and FtsZ assembly (17). Previous studies showed that the CT17 is conserved across a system of FtsZ orthologs, whereas the CTL is hypervariable with significant variations in lengths, amino acid composition, and linear sequence features (56). Here, we used simulations to identify specific inter-module interactions between the CT17 and the T7 loop in *Bs*-FtsZ. We also find that the CTL interacts with regions of the core domain that are non-overlapping with the CT17. The identified interactions among the three modules can be extrapolated to intermolecular interactions among modules in *trans* across multiple FtsZ subunits. These interactions are likely to contribute to lateral associations of FtsZ protofilaments.

Considerable attention has focused on the lengths of CTLs and their impacts on FtsZ functions (80, 87-89). Conclusions from such studies can be confounding because the CTLs are not simple homopolymers. As a result, titrating lengths in arbitrary ways, creates a multivariable problem where the composition and patterning of residues are also varied, thereby confounding the inferred relationships between length and function. To avoid such problems, we focused on a single sequence parameter κ_{+-} whereby we fixed the length and amino acid composition and directly modulated the interplay between intra- and intermolecular interactions. Our results show that changes to sequence patterns within the CTL have clear biophysical, biochemical, and biological consequences. We observe deleterious consequences in FtsZ functionalities when the oppositely charged residues of the CTL are segregated with CTT κ_{+-} values greater than 0.34 leading to aberrant assemblies. This gain-of-function affects both the CTT-core and CTT-CTT interactions between FtsZ molecules. Our results suggest that the loss of native interactions between the T7 loop and the CT17 can be detrimental, as seen for K47. In contrast, the preservation of native contacts in K59 helps maintain WT-like functions *in vivo* because the cognate autoinhibitory interactions are maintained for these variants.

Taken together, our results suggest that the drive to limit interactions between the CTL and the core is conserved in FtsZ orthologs. This is achieved via non-random segregation of negatively charged residues, and dispersion of positively charged residues along the CTL sequences. These features contribute to the minimization of associations that lead to aberrant multivalent interactions amongst segregated blocks of charge within CTTs, and between the CTT and core. Although we focused on titrating the linear segregation / mixing of oppositely charged residues, one can imagine a generalization of our approach that uses sequence libraries or directed evolution to query how large- and small-scale changes to conserved sequence patterns alter the functionalities IDRs. Such an approach was deployed in recent studies to identify rules underlying how disordered transactivation domains of transcription factors work (69). Investigations of additional sequence variants that impact the conformational ensemble via alternative CTL-mediated interactions (i.e., polar or polyglutamine tracts (90, 91)) will be helpful to assess the impact of different types of polar interactions.

Our findings indicate that along with composition and length, an optimal CTL requires the balancing of strengths of inter-module interactions in *cis* and in *trans*, the non-random / random sequence patterns, and conserved sequence-ensemble relationships (56). Indeed, the CTT / CTL encoded effects may need to be just right – a Goldilocks effect – given that the CTT and its two distinct modules play multiple regulatory roles. Similar results have been uncovered from deep mutational scans of sequence features of the disordered transactivation domain of Gcn4, which is an essential transcription factor in yeast (69), and in a recent study of hypervariable linkers within viruses. Our investigations open the door for systematic high-throughput experiments that can be applied to other enzymes with N- and C-terminal IDRs to uncover the combination of conserved sequence features that contribute to the functionalities influenced by IDPs / IDRs that are apparently hypervariable, at least in so far as alignment and covariation-based analyses are concerned. Additionally, mechanistic investigations, focused on the effects of the CTL on heterotypic, CT17-mediated interactions will be important to understand how the CTL and CT17 work together to influence interactions in *trans*.

Materials and Methods

General Methods

All *B. subtilis* strains were derived from the strain JH642 (92). Cloning and genetic manipulation were performed using standard techniques (93, 94). All cloning was done using the *E. coli* strain AG1111 derivative PL930 (95). PL930 contains the low copy plasmid pBS58 expressing *E. coli* ftsQAZ, which facilitates cloning of *B. subtilis* FtsZ. Vent DNA polymerase was used for PCR (New England Biolabs). All restriction enzymes and T4 DNA ligase were purchased from New England Biolabs. All genomic DNA extractions were performed using the Wizard Genomic DNA Purification Kit (Promega). Plasmid preparations were made using the NucleoSpin Plasmid Kit (Macherey-Negel). Gel/PCR purifications were performed using the NucleoSpin Gel and PCR Clean-up Kit (Macherey-Negel). Cells were grown in Luria-Bertani (LB) medium at 37 ºC unless otherwise noted. Antibiotics were used at the following concentrations: ampicillin = 100 µg ml^{-1}, spectinomycin = 100 µg ml^{-1}, chloramphenicol = 5 µg ml^{-1}.

Cloning

Synthetic oligonucleotides of the Kappa variants were synthesized (Integrated DNA Technologies) and PCR amplified, restriction digested, and inserted into pPJ19, which contains FtsZ under the control of the P_{spac} promoter that is inducible with IPTG, with restriction sites flanking the CTL. A BamHI site after residue 315 and an XmaI site before residue 366 result in the insertion of amino acid pairs GS and PG N- and C-terminal to the CTL, respectively. All DNA sequences were confirmed by Sanger sequencing.

Strain construction

The Kappa variant strains were constructed as described previously (49, 57). Strains and plasmids used in this study are listed in **Table S1.** They were constructed by first transforming plasmids into wild-type JH642 cells. This strain permits depletion of wild-type FtsZ and is xylose-dependent for normal growth (96).

Growth conditions

Bacillus subtilis strains were first grown from a single colony overnight in LB containing spectinomycin and xylose to a final concentration of 0.5%. Cells were grown overnight in LB medium at 37°C with 100 µg/mL spectinomycin and 0.5% xylose. They were then diluted 1:100 and grown in fresh LB medium supplemented with 0.5% xylose until OD_{600} reached 0.4-0.5. Cells were then washed twice with LB, diluted 1:100, and grown to mid-log phase in 0.1 mM IPTG.

Immunoblotting

Immunoblotting was performed as described previously (7). The cells were lysed with lysozyme and a Fastprep-24 benchtop homogenizer (MP Biomedicals) with 01.mm silica beads. Loading was normalized to the OD600 after pellet resuspension. After transfer to the blot, total protein was quantified using the Spyro Ruby protein blot stain (Thermo Fisher) and imaged on a Gel Dock EZ Imager (Bio-Rad). The blot was probed using affinity-purified polyclonal rabbit anti-FtsZ antibodies and goat anti-rabbit antibodies conjugated to horseradish peroxidase (Invitrogen). Immunoblots were developed using the ECL Western Blotting detection reagents (Bio-Rad Laboratories) and visualized with the luminescent image analyzer Odyssey Fc Imaging System (LI-COR Biosciences).

Growth Curves

Cells were grown overnight under the same media conditions as the immunoblots in 0.5% xylose, back-diluted 1:100, and grown in 0.5% xylose until the cells reached the mid-log phase. The cells were then washed twice with LB, diluted 1:100, and grown in 0.1 mM IPTG. Starting 1 hour after induction, the OD_{600} was measured approximately every 30 minutes for 7 hours, with later time points taken further apart.

Immunofluorescence microscopy (IFM)

Immunofluorescence microscopy was performed as described previously (49). Cells were grown using the same media conditions overnight in 0.5% xylose, back-diluted 1:100, and grown in 0.5% xylose until the cells reached the mid-log phase. The cells were then washed twice with LB, diluted to OD600 0.025, and grown in 0.1 mM IPTG for five generations (~2.5 hours). The cells were harvested and fixed with 16% paraformaldehyde/0.5% glutaraldehyde. The cells were lysed with 2 mg/mL lysozyme. FtsZ was detected with affinity-purified polyclonal rabbit anti-FtsZ serum combined with goat anti-rabbit serum conjugated to Alexa488 (Life Technologies). Cell walls were stained with wheatgerm agglutinin conjugated to tetramethylrhodamine, and DNA was stained with DAPI. Slides were visualized with an Olympus BX51 microscope with Chroma filters and a Hamamatsu OrcaERG camera. Image capture was performed using Nikon Elements (Nikon Instruments) and analyzed via ImageJ (97). The cell length/Z-ring (L/R) ratio was calculated as previously described (82). The L/R ratio was calculated as the sum of the total cell length of a population of cells divided by the total number of Z-rings in that population. Percent Spirals was calculated as a percent of the sum of all Z rings divided by the total number of FtsZ structures in that population.

Line profiles were drawn across each cell using MicrobeJ plug-in (98) in for ImageJ (97). The intensity profiles were imported and adjusted to subtract background signals. The adjusted profiles were each fitted to a Gaussian using a custom script in MATLAB using: $I(x) = a\exp\left[-\left(\frac{x-b}{c}\right)^2\right]$ where $I(x)$ is the intensity at position x. The fits were constrained to yield

positive values of *a*, *b*, and *c* and ensure that *b* and *c* were always greater than the cell length. Values of *b* were binned at 0.1 μm to construct a histogram, from which values were extracted to plot the cumulative distributive functions (CDF) for each of the Kappa variants.

Protein expression and purification

Kappa variants were cloned into the pET-21b(+) expression vector through *E. coli* strain AG1111. The resulting plasmids were mini-prepped and freshly transformed into C41(DE3) cells and used for protein expression. 500 mL of LB medium was inoculated 1:100 with an overnight culture. Cells were grown at 37 ºC until A_{600} ~0.6, and then the cells were induced with IPTG to a final concentration of 1 mM. Cells were grown for an additional 4 h at 37 ºC, and then cells were harvested by centrifugation, and cell pellets were stored at -80 ºC. Purification was performed as previously described (17, 49). Protein preparations were concentrated using spin concentrators, separated into aliquots, flash frozen on liquid N_2, and stored at –80 ºC. Prior to use in an assay, FtsZ aliquots were thawed on ice and centrifuged to remove any insoluble polymers. FtsZ concentration was then determined using Pierce 660 nm assay (Thermo Fisher Scientific) with porcine tubulin (Cytoskeleton) as a standard.

All-Atom Simulations of CTT Sequence Variants

All-atom Monte Carlo simulations were performed using the ABSINTH implicit solvent model and forcefield paradigm as made available in the CAMPARI simulation package (http://campari.sourceforge.net) (99, 100). Simulations utilized the abs_3.2_opls.prm parameter set in conjunction with optimized parameters for neutralizing and excess Na^+ and Cl^- ions (101). Each of the simulations were performed using spherical droplets with a diameter of 120 Å for isolated peptides and 200 Å for full-length proteins with explicit ions to mimic a concentration of 10 mM NaCl. For isolated peptides, temperature replica-exchange Monte Carlo (T-REMC) (102) was utilized to improve conformational sampling. The temperature schedule ranged from 280 K to 400 K. Ensembles corresponding to a temperature of 340 K were used in the analysis reported in this work. Three independent sets of T-REMC simulations were performed for each Kappa variant. In all, the ensembles for each Kappa variant were extracted from simulations, where each T-REMC simulation deploys 5.5×10^7 Monte Carlo steps. In each simulation, the first 5×10^6 steps were discarded as equilibration. For full length proteins, we used SWISS-MODEL (103, 104) to create a homology model of the *Bs* core from PDB ID: IW5B. The core was initially equilibrated in order to add any missing atoms from the PDB file and make sure bond lengths were consistent with the ABSINTH model. Following the initial equilibration of the core, a single simulation step was performed at 20 K to build in each CTT. Then the end PDB structure from this step was used to generate five distinct full length starting structures. Specifically, the core was frozen such that only side chain moves were allowed and then 20,000 simulation steps at 500 K were performed. The end PDBs from the five simulations were then used as the input structures for the five independent full simulations ran at 340 K. For each full simulation a total of 6.15×10^7 steps were performed with 10^7 discarded as equilibration. Simulation results were analyzed using the MDTraj (105) and CAMPARITraj routines that are available at http://pappulab.wustl.edu/CTraj.html.

UV-CD measurements

CD measurements were carried out using a Jasco 810 spectropolarimeter scanning from 260 nm to 190 nm, with a data pitch of 1 nm and a bandwidth of 1 nm. Four to six accumulations were averaged for each spectrum with a scanning speed of 50 nm/min and a 2-s response time (106). Additional details are described in SI Appendix.

90° Light Scattering Assay

Assembly reactions were performed with 5 μM FtsZ in Buffer MES (50 mM MES, 50 mM KCl, 2.5 mM $MgCl_2$, 1 mM EGTA, pH 6.5) at 30 ºC. Measurements were recorded every quarter of a second. A 1-minute baseline was established before adding 1 mM GTP to the reaction. At least three trials were conducted for each variant. All data were collected and exported into Microsoft Excel, and the subsequent analysis was performed using MATLAB. The average baseline was subtracted from each data point.

Transmission Electron Microscopy (TEM)

Samples were prepared in conditions mimicking the light scattering assays, with a lower concentration of 2.5 μM FtsZ to visualize FtsZ filaments. Grids (Ted Pella, Inc.) were glow discharged before use. Before preparing the grids, each sample was incubated for 10 minutes in the presence of 1 mM GTP at 30 ºC to allow for adequate assembly. Each sample was stained three times with 2% uranyl acetate for 20-seconds each. Each staining involved wicking the solution away and waiting 10 seconds in between stains. Samples were visualized using an JEOL JEM-1400 120kV Transmission Electron Microscope (TEM). Images were adjusted in contrast and brightness.

GTPase Activity Assay

GTP hydrolysis activity was measured using a continuous, regenerative coupled GTPase assay (107). In 96-well plates, 5 μM FtsZ in Buffer MES was used, supplemented with 1 mM phosphoenolpyruvate, 250 μM NADH, and 40 units ml^{-1} of pyruvate kinase/lactic dehydrogenase from rabbit muscle (Millipore Sigma) at 30 ºC. A linear decline of NADH absorbance at 340 nm was monitored over 30 minutes using a SpectraMax i3x Multi-Mode Microplate Reader (Molecular Devices). Rate of GTP hydrolysis was calculated from the raw data of A_{340} min^{-1} and normalized to the hydrolysis rate of WT FtsZ.

Fluorescence Correlation Spectroscopy (FCS)

Synthesized CTT peptides labeled with tetramethylrhodamine (TMR) labels were used (WatsonBio). Peptides were thawed in containers with desiccant while the surfaces of the 8-well plates (0.17 ± 0.005 mm thickness) were passivated by adding 150 μL of BSA (2 mg/ml) to the wells and letting it sit for 10-15 minutes. After 15 minutes, the surfaces were washed 3-5x with 1 mL of DI water. Three stocks were generated by dilution in Buffer MES, assumed to have the same viscosity as water: (1) 50 nM peptide, (2) 5 nM peptide, (3) 5 nM free dye. The free dye was used to determine the hydrodynamic radius of the beam and used to calculate the hydrodynamic radius (R_h) of the peptides per the Stokes-Einstein Equation (108). The diffusion coefficient of TMR with the instrument setup used here is 4.30 x 10^{-10} m^2s^{-1}. All data were collected on a Confocor II LSM system (Carl Zeiss-Evotec, Jena, Germany) with a 40x water-immersion objective. Samples were excited at 500 nm, and emission was collected at 620 nm. Data for fluorescence intensity autocorrelation functions were analyzed with Zeiss Confocor II FCS software.

Shannon Entropy Calculations

Shannon entropies were quantified as previously described (56). Here, only two- parameter distributions were used with R_g and δ*. R_g was divided by $n^{0.5}$ where n is the number of residues in each CTT sequence. This accounts for the difference in number of 4 residues between CTT variants and the WT-CTT. For each sequence-specific distribution, we tiled the shape (δ*) - and

size (R_g) -axes into four evenly sized regions, giving rise to a total of 16 bins. The boundaries for each of the bins were computed using the maximum and minimum observed values across all variants.

Acknowledgments

We thank Stephen Vadia and Catherine Kornacki for cloning and strain constructions. TEM imaging was performed in part using the Washington University Center for Cellular Imaging (WUCCI) supported by Washington University School of Medicine, The Children's Discovery Institute of Washington University and St. Louis Children's Hospital (CDI-CORE-2015-505 and CDI-CORE-2019-813) and the Foundation for Barnes-Jewish Hospital (3770 and 4642). MKS is a Center for Science & Engineering of Living Systems (CSELS) postdoctoral fellow at Washington University in St. Louis. This work was also supported by the Air Force Office of Scientific Research (FA9550-20-1-0241) and the US National Science Foundation (MCB1614766) to RVP.

References

1. S. Brodsky, T. Jana, N. Barkai, Order through disorder: The role of intrinsically disordered regions in transcription factor binding specificity. *Current Opinion in Structural Biology* **71**, 110-115 (2021).

2. N. Morffy, L. C. Strader, Structural Aspects of Auxin Signaling. *Cold Spring Harbor Perspectives in Biology* **14**, a039883 (2022).

3. H. J. Dyson, P. E. Wright, NMR illuminates intrinsic disorder. *Current Opinion in Structural Biology* **70**, 44-52 (2021).

4. S. E. Bondos, A. K. Dunker, V. N. Uversky, Intrinsically disordered proteins play diverse roles in cell signaling. *Cell Communication and Signaling* **20**, 20 (2022).

5. G. Desjardins *et al.*, Synergy of aromatic residues and phosphoserines within the intrinsically disordered DNA-binding inhibitory elements of the Ets-1 transcription factor. *Proceedings of the National Academy of Sciences USA* **111**, 11019-11024 (2014).

6. S. L. Currie *et al.*, Structured and disordered regions cooperatively mediate DNA-binding autoinhibition of ETS factors ETV1, ETV4 and ETV5. *Nucleic Acids Research* **45**, 2223-2241 (2017).

7. K. Bugge *et al.*, Interactions by Disorder – A Matter of Context. *Frontiers in Molecular Biosciences* **7** (2020).

8. A. Mittal, A. S. Holehouse, M. C. Cohan, R. V. Pappu, Sequence-to-Conformation Relationships of Disordered Regions Tethered to Folded Domains of Proteins. *Journal of Molecular Biology* **430**, 2403-2421 (2018).

9. K. Chen, J. Li, C. Wang, Z. Wei, M. Zhang, Autoinhibition of ankyrin-B/G membrane target bindings by intrinsically disordered segments from the tail regions. *eLife* **6**, e29150 (2017).

10. C. Perez-Borrajero *et al.*, The Biophysical Basis for Phosphorylation-Enhanced DNA-Binding Autoinhibition of the ETS1 Transcription Factor. *Journal of Molecular Biology* **431**, 593-614 (2019).

11. H.-S. Kang *et al.*, An autoinhibitory intramolecular interaction proof-reads RNA recognition by the essential splicing factor U2AF2. *Proceedings of the National Academy of Sciences USA* **117**, 7140-7149 (2020).

12. J. Guillén-Boixet *et al.*, RNA-Induced Conformational Switching and Clustering of G3BP Drive Stress Granule Assembly by Condensation. *Cell* **181**, 346-361.e317 (2020).

13. J. H. Yeon, F. Heinkel, M. Sung, D. Na, J. Gsponer, Systems-wide Identification of cis Regulatory Elements in Proteins. *Cell Systems* **2**, 89-100 (2016).

14. D. R. Paquette, R. W. Tibble, T. S. Daifuku, J. D. Gross, Control of mRNA decapping by autoinhibition. *Nucleic Acids Research* **46**, 6318-6329 (2018).

15. M. Bista, M. Petrovich, A. R. Fersht, MDMX contains an autoinhibitory sequence element. *Proceedings of the National Academy of Sciences USA* **110**, 17814-17819 (2013).

16. S. S. Taylor *et al.*, The Tails of Protein Kinase A. *Molecular Pharmacology* **101**, 219 (2022).

17. M. C. Cohan, A. M. P. Eddelbuettel, P. A. Levin, R. V. Pappu, Dissecting the Functional Contributions of the Intrinsically Disordered C-terminal Tail of Bacillus subtilis FtsZ. *Journal of Molecular Biology* **432**, 3205-3221 (2020).

18. A. F. Straight, C. M. Field, Microtubules, membranes and cytokinesis. *Current Biology* **10**, R760-770 (2000).

19. D. P. Haeusser, W. Margolin, Splitsville: structural and functional insights into the dynamic bacterial Z ring. *Nature Reviews in Microbiology* **14**, 305-319 (2016).

20. N. Tolliday, N. Bouquin, R. Li, Assembly and regulation of the cytokinetic apparatus in budding yeast. *Current Opinion in Microbiology* **4**, 690-695 (2001).

21. T. M. Huckaba, L. A. Pon, Cytokinesis: rho and formins are the ringleaders. *Current Biology* **12**, R813-814 (2002).

22. F. Baluska, D. Menzel, P. W. Barlow, Cytokinesis in plant and animal cells: endosomes 'shut the door'. *Developmental Biology* **294**, 1-10 (2006).

23. J. Guizetti, D. W. Gerlich, Cytokinetic abscission in animal cells. *Seminars in Cell and Developmental Biology* **21**, 909-916 (2010).

24. S. A. Rincon, A. Paoletti, Molecular control of fission yeast cytokinesis. *Seminars in Cell and Developmental Biology* **53**, 28-38 (2016).

25. C. Thieleke-Matos, D. S. Osorio, A. X. Carvalho, E. Morais-de-Sa, Emerging Mechanisms and Roles for Asymmetric Cytokinesis. *International Reviews in Cell and Molecular Biology* **332**, 297-345 (2017).

26. C. Addi, J. Bai, A. Echard, Actin, microtubule, septin and ESCRT filament remodeling during late steps of cytokinesis. *Current Opinion in Cell Biology* **50**, 27-34 (2018).

27. J. Lutkenhaus, FtsZ ring in bacterial cytokinesis. *Molecular Micriobiology* **9**, 403-409 (1993).

28. L. Rothfield, S. Justice, J. Garcia-Lara, Bacterial cell division. *Annual Review of Genetics* **33**, 423-448 (1999).

29. A. Janakiraman, M. B. Goldberg, Recent advances on the development of bacterial poles. *Trends in Microbiology* **12**, 518-525 (2004).

30. H. P. Erickson, D. E. Anderson, M. Osawa, FtsZ in bacterial cytokinesis: cytoskeleton and force generator all in one. *Microbiology and Molecular Biology Reviews* **74**, 504-528 (2010).

31. K. H. Huang, J. Durand-Heredia, A. Janakiraman, FtsZ ring stability: of bundles, tubules, crosslinks, and curves. *Journal of Bacteriology* **195**, 1859-1868 (2013).

32. E. L. Meier, E. D. Goley, Form and function of the bacterial cytokinetic ring. *Current Opinion in Cell Biology* **26**, 19-27 (2014).

33. P. J. Buske, A. Mittal, R. V. Pappu, P. A. Levin, An intrinsically disordered linker plays a critical role in bacterial cell division. *Seminars in Cell and Developmental Biology* **37**, 3-10 (2015).

34. A. W. Bisson-Filho *et al.*, Treadmilling by FtsZ filaments drives peptidoglycan synthesis and bacterial cell division. *Science* **355**, 739-743 (2017).

35. J. M. Monteiro *et al.*, Peptidoglycan synthesis drives an FtsZ-treadmilling-independent step of cytokinesis. *Nature* **554**, 528-532 (2018).

36. D. W. Adams, J. Errington, Bacterial cell division: assembly, maintenance and disassembly of the Z ring. *Nature Reviews in Microbiology* **7**, 642-653 (2009).

37. A. J. F. Egan, W. Vollmer, The physiology of bacterial cell division. *Annals of the New York Academy of Sciences* **1277**, 8-28 (2013).

38. J. Lutkenhaus, The ParA/MinD family puts things in their place. *Trends in Microbiology* **20**, 411-418 (2012).

39. B. Soderstrom, D. O. Daley, The bacterial divisome: more than a ring? *Current Genetics* **63**, 161-164 (2017).

40. D. E. Anderson, F. J. Gueiros-Filho, H. P. Erickson, Assembly dynamics of FtsZ rings in Bacillus subtilis and Escherichia coli and effects of FtsZ-regulating proteins. *Journal of Bacteriology* **186**, 5775-5781 (2004).

41. S. C. Greer, Reversible polymerizations and aggregations. *Annual Review of Physical Chemistry* **53**, 173-200 (2002).

42. L. Romberg, M. Simon, H. P. Erickson, Polymerization of Ftsz, a bacterial homolog of tubulin. is assembly cooperative? *J Biol Chem* **276**, 11743-11753 (2001).

43. M. R. Caplan, H. P. Erickson, Apparent cooperative assembly of the bacterial cell division protein FtsZ demonstrated by isothermal titration calorimetry. *J Biol Chem* **278**, 13784-13788 (2003).

44. T. Matsui, X. Han, J. Yu, M. Yao, I. Tanaka, Structural change in FtsZ Induced by intermolecular interactions between bound GTP and the T7 loop. *J Biol Chem* **289**, 3501-3509 (2014).

45. J. M. Wagstaff *et al.*, A Polymerization-Associated Structural Switch in FtsZ That Enables Treadmilling of Model Filaments. *mBio* **8** (2017).

46. E. R. Miraldi, P. J. Thomas, L. Romberg, Allosteric models for cooperative polymerization of linear polymers. *Biophys J* **95**, 2470-2486 (2008).

47. L. C. Corbin, H. P. Erickson, A Unified Model for Treadmilling and Nucleation of Single-Stranded FtsZ Protofilaments. *Biophys J* **119**, 792-805 (2020).

48. M. A. Oliva, D. Trambaiolo, J. Lowe, Structural insights into the conformational variability of FtsZ. *Journal of Molecular Biology* **373**, 1229-1242 (2007).

49. P. J. Buske, P. A. Levin, Extreme C terminus of bacterial cytoskeletal protein FtsZ plays fundamental role in assembly independent of modulatory proteins. *Journal of Biological Chemistry* **287**, 10945-10957 (2012).

50. S. Vaughan, B. Wickstead, K. Gull, S. G. Addinall, Molecular evolution of FtsZ protein sequences encoded within the genomes of archaea, bacteria, and eukaryota. *J Mol Evol* **58**, 19-29 (2004).

51. M. A. Schumacher, K. H. Huang, W. Zeng, A. Janakiraman, Structure of the Z Ring-associated Protein, ZapD, Bound to the C-terminal Domain of the Tubulin-like Protein, FtsZ, Suggests Mechanism of Z Ring Stabilization through FtsZ Cross-linking. *Journal of Biological Chemistry* **292**, 3740-3750 (2017).

52. M. A. Schumacher, W. Zeng, Structures of the nucleoid occlusion protein SlmA bound to DNA and the C-terminal domain of the cytoskeletal protein FtsZ. *Proceedings of the National Academy of Sciences USA* **113**, 4988-4993 (2016).

53. L. Mosyak *et al.*, The bacterial cell-division protein ZipA and its interaction with an FtsZ fragment revealed by X-ray crystallography. *EMBO Journal* **19**, 3179-3191 (2000).

54. A. Mohan *et al.*, Analysis of Molecular Recognition Features (MoRFs). *Journal of Molecular Biology* **362**, 1043-1059 (2006).

55. P. J. Buske, A. Mittal, R. V. Pappu, P. A. Levin, An intrinsically disordered linker plays a critical role in bacterial cell division. *Semin Cell Dev Biol* **37**, 3-10 (2015).

56. M. C. Cohan, K. M. Ruff, R. V. Pappu, Information theoretic measures for quantifying sequence-ensemble relationships of intrinsically disordered proteins. *Protein Engineering Design & Selection* **32**, 191-202 (2019).

57. P. J. Buske, P. A. Levin, A flexible C-terminal linker is required for proper FtsZ assembly in vitro and cytokinetic ring formation in vivo. *Molecular Micriobiology* **89**, 249-263 (2013).

58. J. Lowe, L. A. Amos, Crystal structure of the bacterial cell-division protein FtsZ. *Nature* **391**, 203-206 (1998).

59. M. A. Schumacher, T. Ohashi, L. Corbin, H. P. Erickson, High-resolution crystal structures of Escherichia coli FtsZ bound to GDP and GTP. *Acta Crystallogr F Struct Biol Commun* **76**, 94-102 (2020).

60. B. Jindal, D. Panda, Understanding FtsZ assembly: cues from the behavior of its N- and C-terminal domains. *Biochemistry* **52**, 7071-7081 (2013).

61. M. C. Cohan, Shinn, M. K., Lalmansingh, J. M., Pappu, R. V., Uncovering non-random binary patterns within sequences of intrinsically disordered proteins. *Journal of Molecular Biology* **434**, 167373 (2022).

62. R. K. Das, R. V. Pappu, Conformations of intrinsically disordered proteins are influenced by linear sequence distributions of oppositely charged residues. *Proceedings of the National Academy of Sciences USA* **110**, 13392-13397 (2013).

63. G. Erdos, M. Pajkos, Z. Dosztanyi, IUPred3: prediction of protein disorder enhanced with unambiguous experimental annotation and visualization of evolutionary conservation. *Nucleic Acids Research* **49**, W297-W303 (2021).

64. Y. Cheng *et al.*, Mining alpha-helix-forming molecular recognition features with cross species sequence alignments. *Biochemistry* **46**, 13468-13477 (2007).

65. C. J. Oldfield *et al.*, Coupled folding and binding with alpha-helix-forming molecular recognition elements. *Biochemistry* **44**, 12454-12470 (2005).

66. N. A. Baker, D. Sept, S. Joseph, J. Holst Michael, J. A. McCammon, Electrostatics of nanosystems: Application to microtubules and the ribosome. *Proceedings of the National Academy of Sciences USA* **98**, 10037-10041 (2001).

67. M. C. Cohan, Shinn, M. K., Lalmansingh, J. M., Pappu, R. V., Uncovering non-random binary patterns within sequences of intrinsically disordered proteins. *Journal of Molecular Biolog* (2021).

68. K. P. Sherry, R. K. Das, R. V. Pappu, D. Barrick, Control of transcriptional activity by design of charge patterning in the intrinsically disordered RAM region of the Notch receptor. *Proceedings of the National Academy of Sciences USA* **114**, E9243-E9252 (2017).

69. M. V. Staller *et al.*, A High-Throughput Mutational Scan of an Intrinsically Disordered Acidic Transcriptional Activation Domain. *Cell Systems* **6**, 444-455 e446 (2018).

70. L. Sawle, J. Huihui, K. Ghosh, All-Atom Simulations Reveal Protein Charge Decoration in the Folded and Unfolded Ensemble Is Key in Thermophilic Adaptation. *Journal of Chemical Theory and Computation* **13**, 5065-5075 (2017).

71. L. Sawle, K. Ghosh, A theoretical method to compute sequence dependent configurational properties in charged polymers and proteins. *Journal of Chemical Physics* **143**, 085101 (2015).

72. R. K. Das, Y. Huang, A. H. Phillips, R. W. Kriwacki, R. V. Pappu, Cryptic sequence features within the disordered protein p27Kip1 regulate cell cycle signaling. *Proceedings of the National Academy of Sciences USA* **113**, 5616-5621 (2016).

73. I. Taneja, A. S. Holehouse, Folded domain charge properties influence the conformational behavior of disordered tails. *Current Research in Structural Biology* **3**, 216-228 (2021).

74. M. E. Gundogdu *et al.*, Large ring polymers align FtsZ polymers for normal septum formation. *EMBO J* **30**, 617-626 (2011).

75. D. Popp, M. Iwasa, A. Narita, H. P. Erickson, Y. Maeda, FtsZ condensates: an in vitro electron microscopy study. *Biopolymers* **91**, 340-350 (2009).

76. F. J. Gueiros-Filho, R. Losick, A widely conserved bacterial cell division protein that promotes assembly of the tubulin-like protein FtsZ. *Genes Dev* **16**, 2544-2556 (2002).

77. A. Mukherjee, J. Lutkenhaus, Analysis of FtsZ assembly by light scattering and determination of the role of divalent metal cations. *J Bacteriol* **181**, 823-832 (1999).

78. G. Fu *et al.*, In vivo structure of the E. coli FtsZ-ring revealed by photoactivated localization microscopy (PALM). *PLoS One* **5**, e12682 (2010).

79. F. Guan *et al.*, Lateral interactions between protofilaments of the bacterial tubulin homolog FtsZ are essential for cell division. *Elife* **7** (2018).

80. S. Huecas *et al.*, Self-Organization of FtsZ Polymers in Solution Reveals Spacer Role of the Disordered C-Terminal Tail. *Biophysical Journal* **113**, 1831-1844 (2017).

81. H. A. Arjes *et al.*, Failsafe mechanisms couple division and DNA replication in bacteria. *Current Biology* **24**, 2149-2155 (2014).

82. R. B. Weart *et al.*, A metabolic sensor governing cell size in bacteria. *Cell* **130**, 335-347 (2007).

83. G. R. Squyres *et al.*, Single-molecule imaging reveals that Z-ring condensation is essential for cell division in Bacillus subtilis. *Nature Microbiology* **6**, 553-562 (2021).

84. K. A. Michie, L. G. Monahan, P. L. Beech, E. J. Harry, Trapping of a spiral-like intermediate of the bacterial cytokinetic protein FtsZ. *Journal of Bacteriology* **188**, 1680-1690 (2006).

85. S. Ben-Yehuda, R. Losick, Asymmetric cell division in B. subtilis involves a spiral-like intermediate of the cytokinetic protein FtsZ. *Cell* **109**, 257-266 (2002).

86. X. Ma, W. Margolin, Genetic and functional analyses of the conserved C-terminal core domain of Escherichia coli FtsZ. *Journal of Bacteriology* **181**, 7531-7544 (1999).

87. K. Sundararajan *et al.*, The bacterial tubulin FtsZ requires its intrinsically disordered linker to direct robust cell wall construction. *Nature Communications* **6**, 7281 (2015).

88. K. A. Gardner, D. A. Moore, H. P. Erickson, The C-terminal linker of Escherichia coli FtsZ functions as an intrinsically disordered peptide. *Molecular Micriobiology* **89**, 264-275 (2013).

89. J. M. Barrows, K. Sundararajan, A. Bhargava, E. D. Goley, FtsA Regulates Z-Ring Morphology and Cell Wall Metabolism in an FtsZ C-Terminal Linker-Dependent Manner in Caulobacter crescentus. *Journal of Bacteriology* **202** (2020).

90. R. K. Das, K. M. Ruff, R. V. Pappu, Relating sequence encoded information to form and function of intrinsically disordered proteins. *Current Opinion in Structural Biology* **32**, 102-112 (2015).

91. T. E. Williamson, A. Vitalis, S. L. Crick, R. V. Pappu, Modulation of polyglutamine conformations and dimer formation by the N-terminus of huntingtin. *Journal of Molecular Biology* **396**, 1295-1309 (2010).

92. M. Perego, G. B. Spiegelman, J. A. Hoch, Structure of the gene for the transition state regulator, abrB: regulator synthesis is controlled by the spo0A sporulation gene in Bacillus subtilis. *Molecular Micriobiology* **2**, 689-699 (1988).

93. C. R. Harwood, S. M. Cutting, *Molecular biological methods for Bacillus*, Modern microbiological methods (Wiley, Chichester ; New York, 1990), pp. xxxv, 581 p.

94. J. Sambrook, D. W. Russell, *Molecular cloning : a laboratory manual* (Cold Spring Harbor Laboratory Press, Cold Spring Harbor, N.Y., ed. 3rd, 2001).

95. X. Wang, J. Lutkenhaus, The FtsZ protein of Bacillus subtilis is localized at the division site and has GTPase activity that is dependent upon FtsZ concentration. *Molecular Micriobiology* **9**, 435-442 (1993).

96. R. B. Weart, P. A. Levin, Growth rate-dependent regulation of medial FtsZ ring formation. *Journal of Bacteriology* **185**, 2826-2834 (2003).

97. C. A. Schneider, W. S. Rasband, K. W. Eliceiri, NIH Image to ImageJ: 25 years of image analysis. *Nature Methods* **9**, 671-675 (2012).

98. A. Ducret, E. M. Quardokus, Y. V. Brun, MicrobeJ, a tool for high throughput bacterial cell detection and quantitative analysis. *Nature Microbiology* **1**, 16077 (2016).

99. A. Vitalis, R. V. Pappu, Methods for Monte Carlo simulations of biomacromolecules. *Annual Reports in Computational Chemistry* **5**, 49-76 (2009).

100. A. Radhakrishnan, A. Vitalis, A. H. Mao, A. T. Steffen, R. V. Pappu, Improved atomistic Monte Carlo simulations demonstrate that poly-L-proline adopts heterogeneous ensembles of conformations of semi-rigid segments interrupted by kinks. *Journal of Physical Chemistry B* **116**, 6862-6871 (2012).

101. A. H. Mao, R. V. Pappu, Crystal lattice properties fully determine short-range interaction parameters for alkali and halide ions. *Journal of Chemical Physics* **137**, 064104 (2012).

102. Y. Sugita, Y. Okamoto, Replica-exchange molecular dynamics method for protein folding. *Chemical Physics Letters* **314(1-2)**, 141-151 (1999).

103. N. Guex, M. C. Peitsch, T. Schwede, Automated comparative protein structure modeling with SWISS-MODEL and Swiss-PdbViewer: a historical perspective. *Electrophoresis* **30 Suppl 1**, S162-173 (2009).

104. A. Waterhouse *et al.*, SWISS-MODEL: homology modelling of protein structures and complexes. *Nucleic Acids Res* **46**, W296-W303 (2018).

105. R. T. McGibbon *et al.*, MDTraj: A Modern Open Library for the Analysis of Molecular Dynamics Trajectories. *Biophysical Journal* **109**, 1528-1532 (2015).

106. I. Seim *et al.*, Dilute phase oligomerization can oppose phase separation and modulate material properties of a ribonucleoprotein condensate. *Proceedings of the National Academy of Sciences USA* **119**, e2120799119 (2022).

107. E. Ingerman, J. Nunnari, A continuous, regenerative coupled GTPase assay for dynamin-related proteins. *Methods in Enzymology* **404**, 611-619 (2005).

108. D. Magde, E. L. Elson, W. W. Webb, Fluorescence correlation spectroscopy. II. An experimental realization. *Biopolymers* **13**, 29-61 (1974).

Supporting Information Appendix

for

Connecting sequence features within the disordered C-terminal linker of *B. subtilis* FtsZ to function and bacterial cell division

Min Kyung Shinn [a], Megan C. Cohan [a], Jessie L. Bullock [b], Kiersten M. Ruff [a,1], Petra A. Levin [b,1], Rohit V. Pappu[a,1]

[a] Department of Biomedical Engineering, Center for Science and Engineering of Living Cells (CSELS), Washington University in St. Louis, St. Louis, MO 63130

[b] Department of Biology, Washington University in St. Louis, St. Louis, MO 63130

[1]To whom correspondence may be addressed. Email: kiersten.ruff@wustl.edu, plevin@wustl.edu, pappu@wustl.edu

Supporting Information Text

UV-CD measurements. A quartz cuvette with a path length of 1 mm was used for all measurements. Buffer MES (50 mM MES, 50 mM KCl, 2.5 mM $MgCl_2$, 1 mM EGTA, pH 6.5) filtered with a 0.2 µm PES filter was used in all measurements at 30 ºC. CD spectra were converted from machine units (mdeg) to mean residue ellipticity ([θ], deg cm^2 $dmol^{-1}$ $residue^{-1}$) as described (1). Peptide concentrations were determined by absorbance using an Implen NP80 nanophotometer. Molar concentration values were calculated using an extinction coefficient of 195 M^{-1} cm^{-1} at 258 nm.

Deconvolution of CD data. CD data sets were converted to units of mean residue ellipticity as described (1) and submitted to the Dichroweb server (2) (http://dichroweb.cryst.bbk.ac.uk) for deconvolution using the CDSSTR algorithm (3) and basis sets 4, 7, and SP175t, which are optimized for the wavelength rage of 190-240 nm (4, 5). We present the α-helical, β-strand, and β-turn categories each as a sum of two sub-categories that are given in the output of the analysis. The plotted secondary structure content estimates represent the mean and standard deviation of the values results obtained from the three basis sets.

Table S1

Variant	Sequence	κ_{+-}
K14	GS HQPKPEQKSEANQSREQVTRELHSRNVPEIQKKDKVPQQPSTNTSTPQRI PG-***CTP***	0.136
K18	GS VQNKQIEKQKEPERRQRTHVESSPHQPSSQPVDRNPLPKTNQTQEKASIT PG-***CTP***	0.182
K20	GS IKQERKVTKPQEPSLNQSIRTHNQSVPEKEPDERRPQQQNTVSKHTSQPA PG-***CTP***	0.197
WT	IEQEKDVTKPQRPSLNQSIKTHNQSVPKREPKREEPQQQNTVSRHTSQPA PG-***CTP***	0.197
K26	GS IEQKEKVTKPQRPSLNQSIETHNQSVPRRKPREKDPQQQNTVSEHTSQPA PG-***CTP***	0.258
K33	GS KQSTNTPQEKQPSIKVRRQQEVKPSLQKQENTVHIRRHSNAPTSDPPEEQ PG-***CTP***	0.331
K34	GS HQKPRQKVNKRQSEIRVPQSELSRSPTQENEEQSQPPAKTKNVQDTIHTP PG-***CTP***	0.332
K41	GS HPPEQQISKTRKRHVTQSQQEDEPPAKQKSLRRQNQEINVVNSSKPETTP PG-***CTP***	0.408
K47	GS PQIHQPKPQKKRSSNPTDQHKSAVTTPRKRVLIRQQPQTESEVEEESNQN PG-***CTP***	0.466
K53	GS IEQEEDVTEPQEPSLNQSIRTHNQSVPKKKPRKKRPQQQNTVSRHTSQPA PG-***CTP***	0.528
K59	GS PIVLEEDEETSEVSTNQKTQQVKPPPINSSQPQQHHPQRAQRKRRKKTSN PG-***CTP***	0.591
K72	GS NSQTQIRKRRKKKKRSSHQIVNLPNAPPDPEEEESEPHQSQTQPTVTQVQ PG-***CTP***	0.717

Table S1: Sequences of the Kappa variants with the conserved CTP motif shown as *CTP*. We designed ten CTT sequences with κ_{+-} values spanning from 0.14 to 0.72. Column 1 shows the name assigned to each *B. subtilis* FtsZ variant; columns 2 and 3 show the designed sequence of the CTL and the κ_{+-} value for the variant, respectively. K33 is identical to previously reported Scr construct (6). Sequences of Kappa variants are 4 residues longer because of the cloning artifacts (see Methods).

Table S2: List of plasmids and strains used in the study.

Strain or Plasmid	Genotype/features	Source
	B. subtilis	
JH642	trpC2 pheA1	Perego et al 1988
PAL 2084	JHC642 thrC::P_{xyl}-ftsZ	Weart Levin 2003
PAL 3171	PAL 2084 amyE::P_{spac}-ftsZ	Buske Levin 2012
PAL 3491	PAL 2084 *amyE*::P_{spac}-*ftsZCTLV1*	This study
PAL 3495	PAL 2084 *amyE*::P_{spac}-*ftsZCTLV2*	This study
PAL 3499	PAL 2084 *amyE*::P_{spac}-*ftsZCTLV3*	This study
PAL 3503	PAL 2084 *amyE*::P_{spac}-*ftsZCTLV4*	This study
PAL 3507	PAL 2084 *amyE*::P_{spac}-*ftsZCTLV5*	This study
PAL 3511	PAL 2084 *amyE*::P_{spac}-*ftsZCTLV6*	This study
VK 1	PAL 2084 *amyE*::P_{spac}-*ftsZK19*	This study
VK 2	PAL 2084 *amyE*::P_{spac}-*ftsZ*K53	This study
VK 3	PAL 2084 *amyE*::P_{spac}-*ftsZK59*	This study
	E. coli	
AG1111	*DZR200- MC1061 F'lacIQ lacZM15 Tn10 (tet)*	Ireton et al 1993
PAL 930	AG1111 + pBS58	Weart Levin 2003
Plasmids		
pPJ19	pET21b(+)-ftsZ946-51 Bam HI 1090-95 XmaI stop	Buske Levin 2013
pPJ53	pET21(+)-*ftsZCTLV1* stop	This study
pPJ54	pdR67-*ftsZCTLV1* stop	This study
pPJ55	pET21(+)-*ftsZCTLV2* stop	This study
pPJ56	pdR67-*ftsZCTLV2* stop	This study
pPJ57	pET21(+)-*ftsZCTLV3* stop	This study
pPJ58	pdR67-*ftsZCTLV3* stop	This study
pPJ59	pET21(+)-*ftsZCTLV4* stop	This study
pPJ60	pdR67-*ftsZCTLV4* stop	This study
pPJ61	pET21(+)-*ftsZCTLV5* stop	This study
pPJ62	pdR67-*ftsZCTLV5* stop	This study
pPJ63	pET21(+)-*ftsZCTLV6* stop	This study
pPJ64	pdR67-*ftsZCTLV6* stop	This study
pVK1	pET21(+)-*ftsZK19* stop	This study
pVK2	pdR67-*ftsZK19* stop	This study
pVK3	pET21(+)-*ftsZK53* stop	This study
pVK4	pdR67-*ftsZK53* stop	This study
pVK5	pET21(+)-*ftsZK59* stop	This study
pVK6	pdR67-*ftsZK59* stop	This study

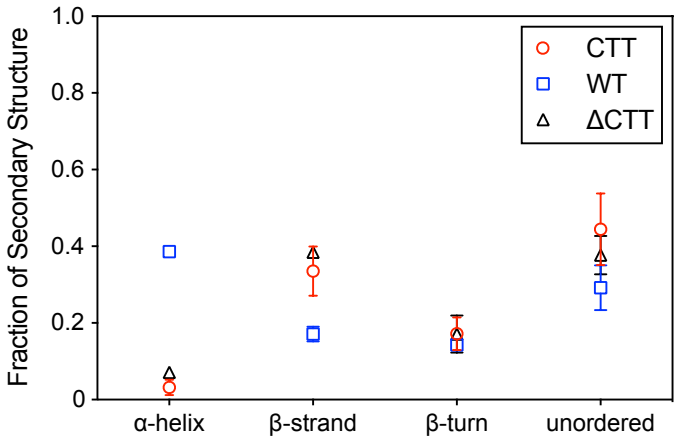

Fig. S1. Secondary structure contents of each construct for CD. Secondary structures were determined by deconvolution using the CDSSTR algorithm and basis sets 4, 7, and SP175t, as implemented by the Dichroweb server. Open circles and error bars represent the mean and standard deviation, respectively, of the analysis resulting from these three basis sets. See SI Methods for details.

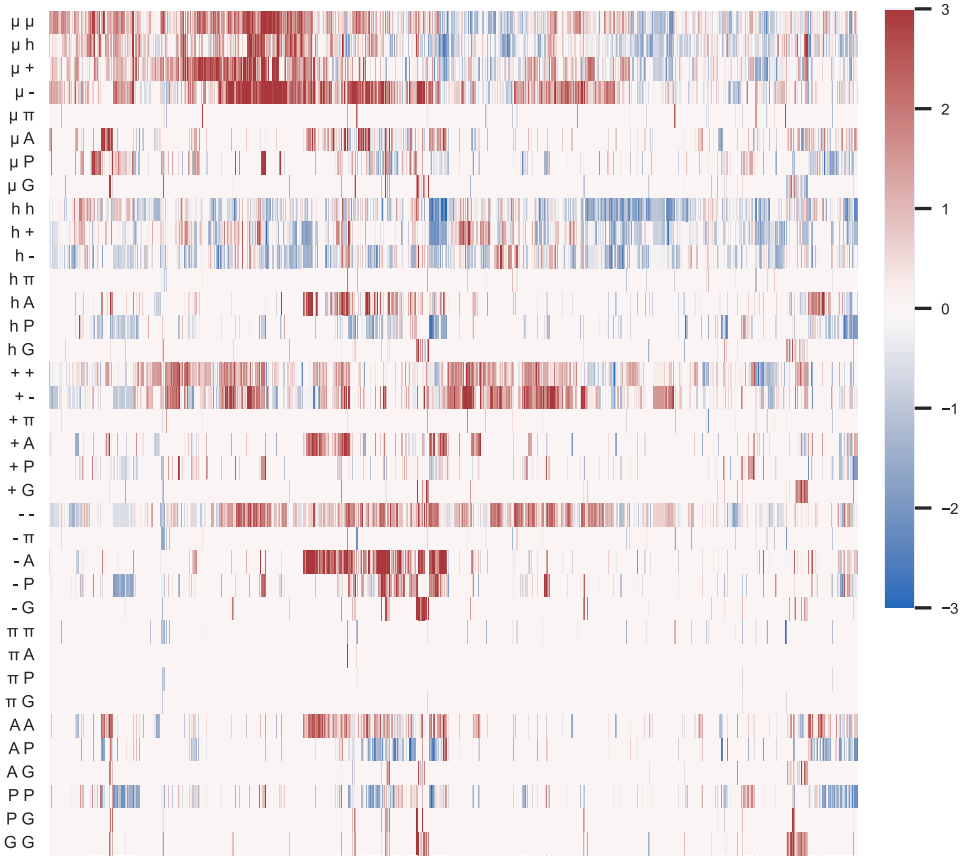

Figure S2: Comparison of linear sequence patterning of the CTTs from 1208 FtsZ orthologs. Each column is a heatmap of z-scores computed across the CTTs of FtsZ orthologs corresponding to the color bar on the right. Conserved non-random features refer to binary patterns that have non-zero z-scores across most of orthologs.

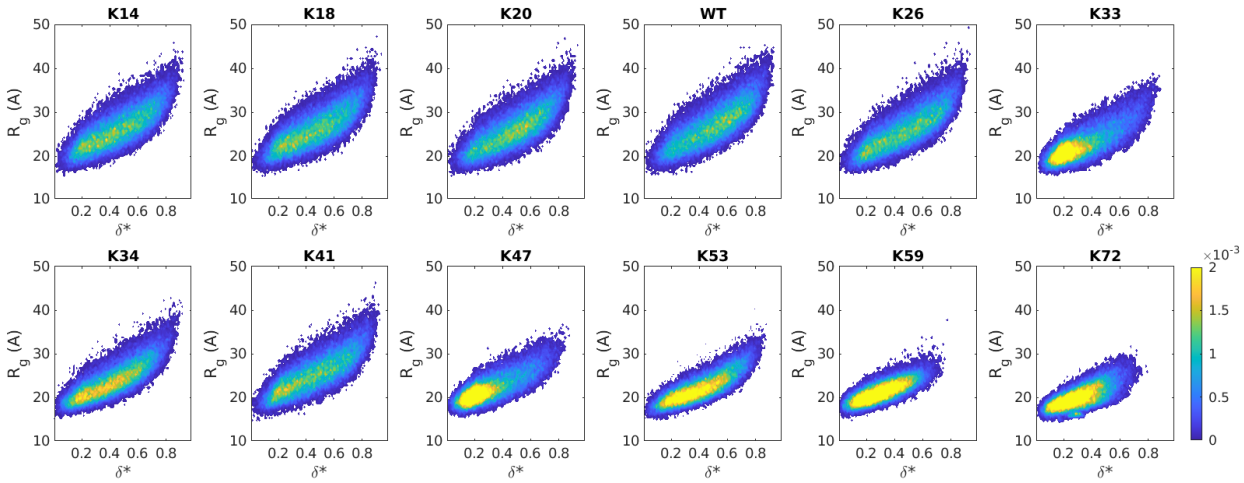

Figure S3: Conformational distributions of isolated CTT peptides of Kappa variants. The figure shows probability density distributions of asphericity (δ*) and R_g obtained from simulations. The color bars show the probability densities. The bin widths along the abscissa and ordinate are 0.01 and 0.5 Å, respectively. Data are shown for simulations performed at a temperature of 340 K. Low values of δ*correspond to globules, intermediate values of δ* correspond to prolate ellipsoids, and values of δ* tending to unit are rod-like conformations. For CTT peptides with $\kappa_{+-} \leq 0.26$, the distributions are relatively flat across the asphericity axis, spanning the range of δ* values from 0.1 – 0.8 and R_g axis ranging from ~ 17 Å – 42 Å. The probability density associated with compact, globular conformations increases as κ_{+-} increases above 0.33.

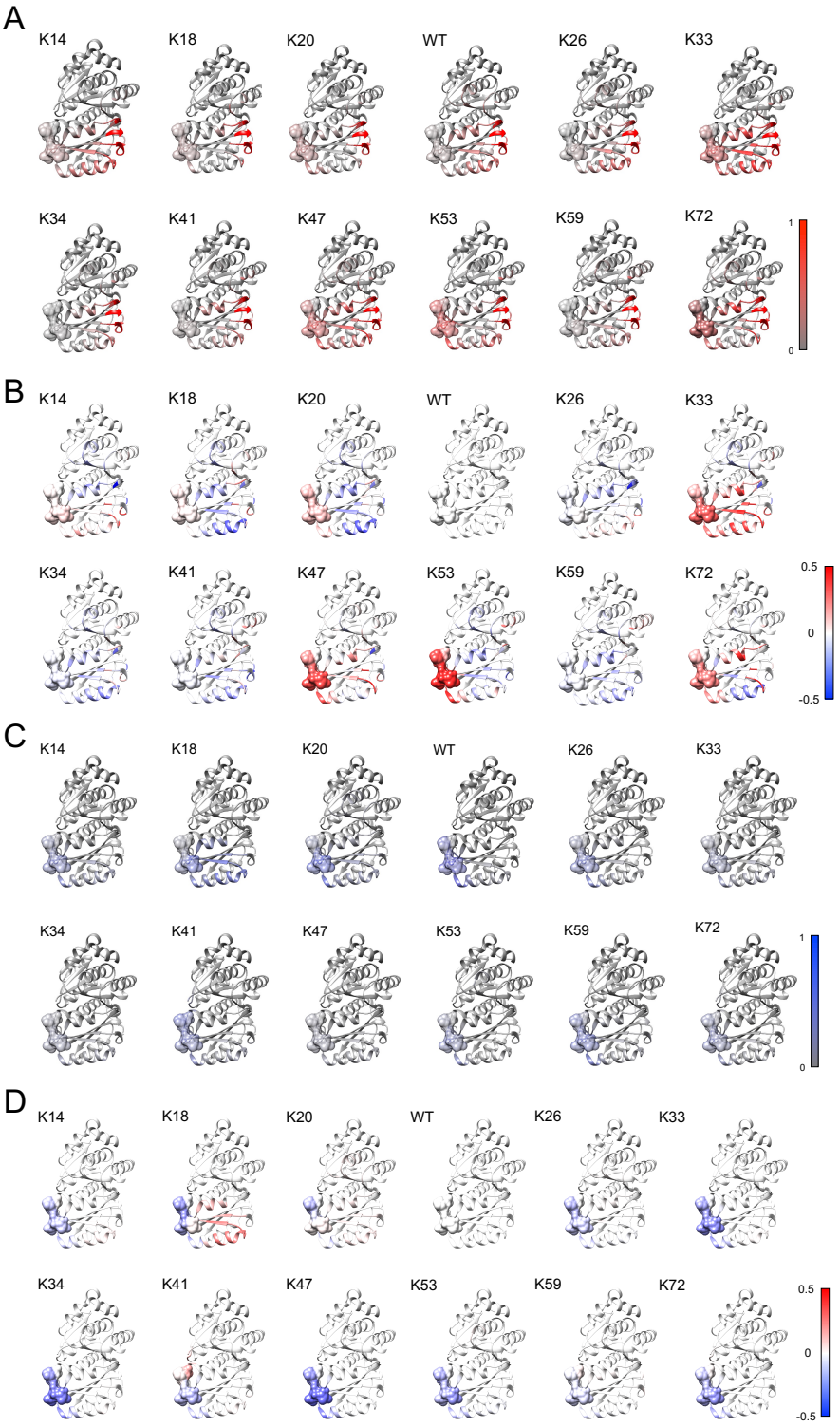

Figure S4 Intra-molecular interactions between the core and CTL or CTP in Kappa variants. The colors on the structures of *Bs*-FtsZ core domain indicate the fractional frequency of (A) CTL or (C) CTP coming within 10 Å of the residues in the core domain as indicated in the color bar on the right. Differences in fractional frequency of (B) CTL-core or (D) CTP-core interactions between each Kappa variant and WT are mapped onto the structure of the core domain.

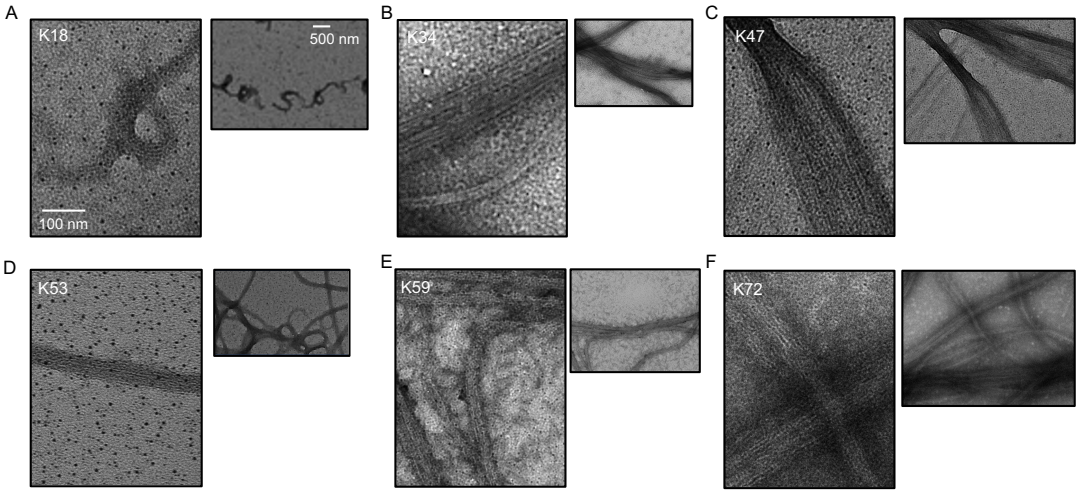

Figure S5: TEM images of select Kappa variants. The Kappa variants presented here were chosen to highlight the non-native, large assemblies formed by what appear to be tail-mediated interactions. Structures. The images are shown using scale bars of 100 nm and 500 nm. These scalebars help highlight show the largeness of the assemblies and the lateral associations of filaments.

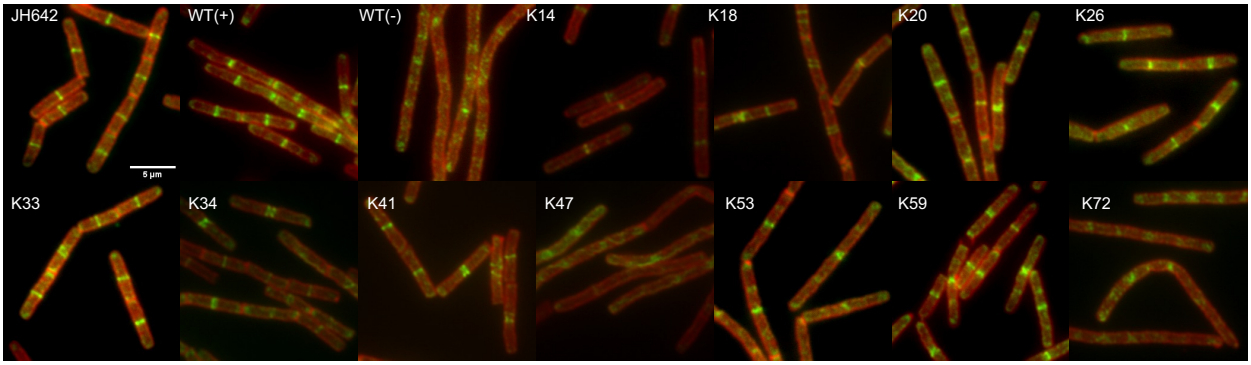

Figure S6: IFM images of representative *B. subtilis* cells expressing Kappa variants. The imaged cells were artificially colored in green for FtsZ and red for the cell wall. The cell septa can be identified by high intensity of red lines between two or more *B. subtilis* cells at their poles.

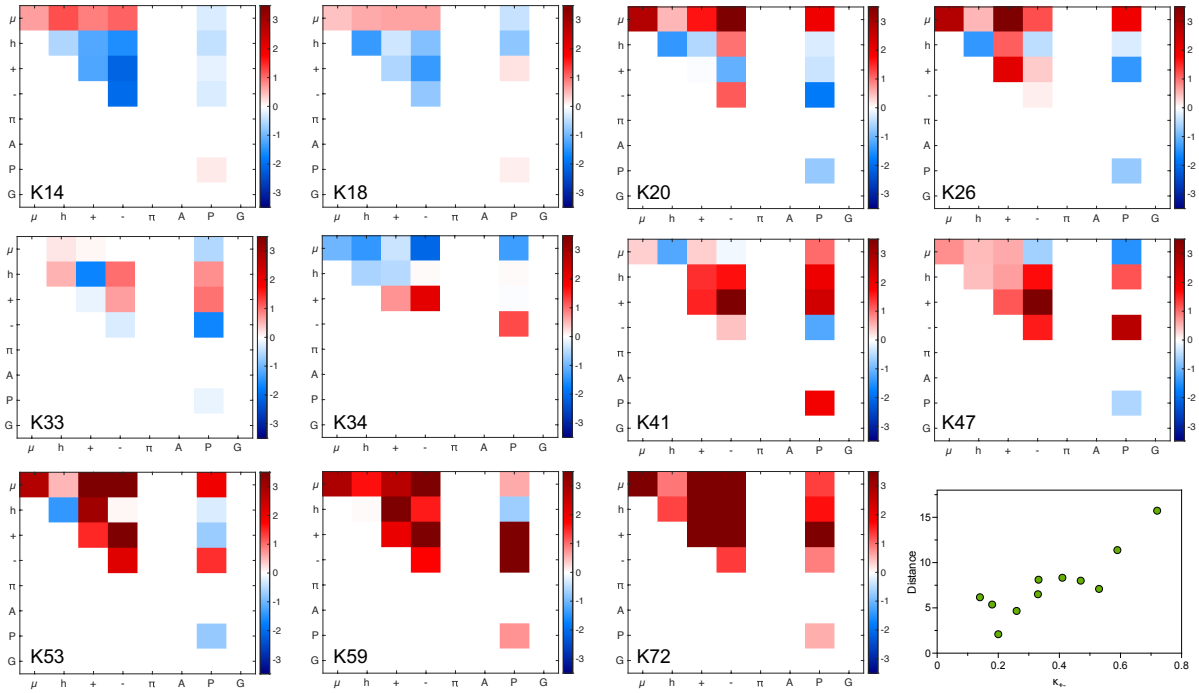

Figure S7: Z-score matrices of CTT sequences for Kappa variants. The data show results from NARDINI analysis. The Euclidean distance between the z-score matrices of the WT CTT and CTTs of Kappa variants show a non-monotonic variation between 0.1 and 0.5.

References

1. I. Seim *et al.*, Dilute phase oligomerization can oppose phase separation and modulate material properties of a ribonucleoprotein condensate. *Proc Natl Acad Sci U S A* **119**, e2120799119 (2022).

2. A. J. Miles, S. G. Ramalli, B. A. Wallace, DichroWeb, a website for calculating protein secondary structure from circular dichroism spectroscopic data. *Protein Sci* **31**, 37-46 (2022).

3. L. A. Compton, W. C. Johnson, Jr., Analysis of protein circular dichroism spectra for secondary structure using a simple matrix multiplication. *Anal Biochem* **155**, 155-167 (1986).

4. N. Sreerama, S. Y. Venyaminov, R. W. Woody, Estimation of protein secondary structure from circular dichroism spectra: inclusion of denatured proteins with native proteins in the analysis. *Anal Biochem* **287**, 243-251 (2000).

5. J. G. Lees, A. J. Miles, F. Wien, B. A. Wallace, A reference database for circular dichroism spectroscopy covering fold and secondary structure space. *Bioinformatics* **22**, 1955-1962 (2006).

6. P. J. Buske, P. A. Levin, A flexible C-terminal linker is required for proper FtsZ assembly in vitro and cytokinetic ring formation in vivo. *Molecular Microbiology* **89**, 249-263 (2013).